Large Eddy Simulation of Land-Atmosphere Interaction

By

JOHN DAVID ALBERTSON
B.S. (State University of New York at Buffalo) 1985
M.B.A. (University of Hartford) 1989
M.E.S. (Yale University) 1993

DISSERTATION

Submitted in partial satisfaction of the requirements for the degree of

DOCTOR OF PHILOSOPHY

in

Hydrologic Science

in the

OFFICE OF GRADUATE STUDIES

of the

UNIVERSITY OF CALIFORNIA

DAVIS

Approved:

_____

_____

_____

Committee in Charge

1996

i

John David Albertson
September, 1996
Hydrologic Science

Large Eddy Simulation of Land-Atmosphere Interaction

Abstract

A large eddy simulation (LES) code of the atmospheric boundary layer (ABL) has been developed to study the effect of spatially variable surface properties on the aerially averaged exchange rates of water vapor, heat, and momentum across the land-atmosphere interface. The LES code simulates the space and time evolution of the large scale turbulent motion in the ABL. As the turbulent fluxes of momentum and scalars are predominately carried by the large scale eddy structures, we are able to use the LES to simulate turbulent flux processes in the ABL. In the first chapter a general review of LES studies of the ABL is presented. In the second chapter the LES theory is outlined and the equations of motion and transport are manipulated to form the LES equations, which are then treated with pseudospectral numerics in the horizontal directions and finite difference numerics in the vertical direction and in time as implemented in the present code. The third chapter examines the performance of the LES code with respect to simulation of the neutrally stratified ABL with a comparison to previously published simulation results. The fourth and final chapter applies the LES code to study the spatial scaling of surface shear stress (i.e. momentum flux across the land-atmosphere interface) over patchy land surfaces for the neutrally stratified ABL. It is shown that the presence of abrupt changes in surface roughness and the atmosphere's response to these patches creates a marked dependence of the statistical structure of surface shear stress on the length scale of the surface patches. Through this dependence we observe a clear increase in spatially averaged surface stress for decreasing patch scale. And finally, implications for scalar exchange are discussed.

CHAPTER 1

Introduction

This work addresses, in general, the exchange of water vapor, heat, and momentum between the land and the atmosphere. This interaction is central to surface-based studies, such as watershed hydrology and regional water management, and to atmosphere-based studies, such as mesoscale dynamics and general circulation modeling for climate change studies. Consequently, the study of land-atmosphere interaction sees an overlap in disciplines from hydrology to meteorology, each concerned with similar processes, but often at different scales. A pressing concern of common interest to these groups is how to deal with the effect of spatially variable surface conditions on areal averaged exchange rates. We see this problem arising in field scale hydrology for the estimation of evaporation rates in water balance studies (Parlange et al., 1995) and in meteorology where the grid-cell averaged exchange rates of water, heat, and momentum are necessary for accurate simulation of short term weather and long term climate phenomena (Haltiner and Williams, 1980; Pielke, 1984). In fact, it is widely held that our ability to predict climate evolution is limited by the crude means by which we presently represent the interaction between the land and the atmosphere (Garratt, 1993). And, on short time scales, improved representation of land-atmosphere fluxes and the role of surface soil moisture is needed to advance the state of numerical weather prediction (Dabberdt and Schlatter, 1996). However, efforts to deal with the spatial variability

of surface properties are frustrated by the extreme range of scales over which the variability is active and the general lack of theory for how these scales are coupled with the scales of motion in the atmosphere.

The general question addressed here is "are all scales of variation in surface properties equally coupled with the atmospheric dynamics with respect to their effects on areal averaged surface fluxes?" This question can not be easily answered from a review of the literature, for while many studies have looked for effects in atmospheric features due to variations in surface conditions, most have neglected the question of what effect the variations have on aerially averaged exchange rates. At one scale extreme, there are documented strong effects on mesoscale motion due to the existence of distinct surface variations (e.g. irrigation in arid region) over scales of $O(10km)$ (e.g. Ookouchi et al., 1984; Michels and Jochum, 1995). These mesoscale effects can be as strong as the sea breeze that sets up across the ocean-land interface (Segal and Arritt, 1992). In the mid-range scales ($100\ m - 10km$) we can expect some degree of impact on surface fluxes from spatial variation in surface conditions because of the feedback effects between surface fluxes and near surface atmospheric properties. Taking evaporation as an example, we note that there is a strong dependence between the actual evaporation and the water vapor deficit in the lower atmosphere. Therefore, extreme evaporation over one field will modify the characteristics of the air, which will in turn affect the flux from the downwind field (e.g. Brutsaert and Stricker, 1979; Parlange and Katul, 1992; Cooper et al., 1992). In discussing this last point, de Bruin (1989) stated that

"future models of regional evapotranspiration will have to account for the effects of surface inhomogeneities on the dynamics of the [atmospheric boundary layer (ABL)]." Moreover, Shen and Leclerc (1995) have identified, through simulations, that surface inhomogeneities on scales smaller than 1000 m can have significant effects on the turbulence structure of the convective boundary layer. And lastly, while we know that significant spatial variability in surface properties is present at small scales ($< 100\ m$) and that these variations may have significant effects for other processes such as subsurface transport (e.g. Ritsema and Dekker, 1995), it is unclear to what degree they are coupled with the atmospheric properties to affect the net surface flux (Baldocchi, 1989).

also in refs.

The basic hypothesis behind this work is that: (i) the larger scales of variability have significant effects on mesoscale dynamics but are largely characterized by an equilibrium between surface patch properties and mean properties of the overlying air, thus the patches have independent effects on the domain averaged exchange rates; (ii) the medium scale patches may not affect circulations but adjacent patches are strongly coupled with respect to surface fluxes as the mean air properties are due to both the upwind surface and the underlying surface; and (iii) patch sizes below some threshold have negligible effects on the mean atmospheric properties and may be handled statistically. If this is true, the study of exchange across the land-atmosphere interface could be focused toward particular ranges of scales of variability, thus potentially decreasing data requirements while increasing the level of comfort in parameter estimation. Therefore, we explore the relation-

ship between scales of surface variability and their degree of coupling with the atmospheric scales with respect to areal averaged surface fluxes. Whereas Shen and Leclerc (1995), *inter alia*, addressed effects on turbulence statistics, this work addresses the specific aspect of effects on net surface exchange of momentum and scalars. This point is addressed more completely in chapter 4, including a more thorough tie to the existing literature.

To address properly this problem would require a vast amount of data covering (i) surface conditions over a wide range of scales of variability, (ii) surface fluxes distributed in space and time, and (iii) the dynamics of interaction between the surface and the atmospheric motions. Furthermore, we would naturally want to be able to control the experiment to identify the basic interaction between the defined ranges of scales on the surface and the broad range of scales in the atmospheric motion above. Data and control such as desired for this problem are obviously unavailable in the field at the scale of interest; and, modeling studies that attempt to address this issue while ignoring atmospheric motion and the inherent feedback mechanisms (e.g. Stewart, 1989; Famiglietti and Wood, 1995) are unable to provide the necessary insight. Furthermore, wind tunnels are unable to simulate adequately the scale and complexity of the convective ABL flows for purposes such as the present one. A promising tool for this situation is the numerical simulation of ABL flows. With numerical simulations we can have absolute control of surface boundary conditions as well as access to any conceivable "data" necessary to diagnose the surface-flow interactions.

Numerical simulation of turbulence is divided into two basic classes: (i) direct numerical simulation (DNS) where all scales of the flow are resolved, from the largest energy producing eddies down to the small energy dissipating eddies; and, (ii) large eddy simulation (LES) where a range of scales is resolved, from the largest eddies down to an arbitrary cut-off point, below which the dynamics are modeled. Resolving the flow implies that the equations of motion are integrated over a discrete mesh in time and space.

The direct numerical simulation of ABL dynamics would require the solution of the governing equations over a grid capable of resolving the dissipation scale of motion. Simple order of magnitude dimensional arguments suggest that this would require resolving $R^{9/4}$ degrees of freedom, where R is the Reynolds number (McComb, 1990). As R can be of order 10^8 in the ABL, this is equivalent to a requirement of approximately 10^{18} nodes (or modes if using spectral methods). Present computing resources limit the size of practical applications to about 10^8 degrees of freedom, putting far out of reach the successful resolution of the dissipation scale within a model of the ABL. Thus the numerical modeling efforts described here are limited to partial resolution of the turbulence through LES. Following is a brief and general discussion of LES including a review of the relevant application literature.

1.1 Large Eddy Simulation

A fundamental tenet of LES is that the large scales of motion are the most dependent upon the gross flow characteristics. These structures are resolved in the

LES, while the eddies smaller than some scale in the inertial subrange are modeled in terms of the resolved scales. This is a natural approach, for while the inertial subrange eddies receive their energy from the larger scales, they are also rendered statistically independent of the large scale motion and any anisotropy that it may possess through the cascading process (e.g. Batchelor, 1953). .

To account for this incomplete resolution, the equations of motion and transport must be modified; for if the dissipation scales are not resolved or otherwise accounted for, the cascading energy would accumulate in the resolved range rather than continuing down scale and ultimately being dissipated by molecular action (see, e.g., Leonard, 1974). The velocity and scalar fields (e.g. temperature and water vapor) are filtered to separate explicitly the resolved from the unresolved parts. Applying the filter to the governing equations yields equations for the resolved scales which contain certain terms involving the unresolved scales. The equations are integrated numerically with the unresolved scales parameterized by a sub-grid (or sub-filter) model, such as the eddy viscosity model pioneered by Smagorinsky (1963).

The equations of motion and transport require initial and boundary conditions. The horizontal directions are typically (but not necessarily) treated with periodic boundary conditions. This is employed explicitly in finite difference LES by "wrapping" the differencing stencil from one boundary around to the other (one may visualize identical flow domains set end-to-end). With Fourier-based spectral methods the periodic boundary conditions are implicit to the underlying

basis functions which, by definition, are periodic. The top boundary is usually positioned well above the height of the ABL, and the stable capping inversion layer serves to keep the flow of interest well isolated from the top boundary. Therefore, the simulation of convective ABL dynamics is relatively insensitive to the top boundary conditions, which usually involve some sort of "no-stress" lid, implying a zero vertical gradient of the velocity at the top of the domain; similar physical arguments are used for the scalars. The bottom boundary, however, is considerably more problematic. This is because as we near the surface an increasingly large amount of the energy and flux is contained in the small unresolved scales and must, therefore, be handled by the sub-grid model. The present state of the science involves the use of relationships such as those based on Monin-Obukhov similarity theory to relate the resolved flow quantities near the boundary to the surface fluxes across the boundary.

Our present focus is on the applications of LES to ABL flows, with particular attention to its prospects for supporting the development and refinement of models of land-atmosphere exchange. Following is a brief review of the literature, divided into studies of the neutral, stable, and convective regimes and studies which specifically address flow over complex terrain.

1.1.1 The Neutral Regime

Neutrally stratified boundary layer flows are difficult to simulate with a partial-resolution approach such as LES since the dominant eddy size scales with the height above the surface. The challenge to simulate this flow is that the important surface layer eddies are often smaller than the

mesh spacing, and the turbulent production is concentrated in the marginally resolved near wall region, whereas for the convective boundary layer production is essentially independent of height. In light of this challenge, the neutral boundary layer provides a stringent test of an LES code. Mason and Thompson (1987) performed a suite of simulations of the neutral boundary layer to investigate both the structure of the turbulence and the effect of mesh resolution on the results. Their simulations depicted an equality of production and dissipation of turbulent kinetic energy (TKE) at moderate heights with an excess of dissipation at the greater heights balanced by a transport of TKE from the lower regions where the strong gradients are known from experimental investigations to produce a local excess of TKE with respect to dissipation (e.g. Albertson et al., 1996a). Four LES codes were compared by Andren et al. (1994) for their performance in simulating the neutrally stratified Ekman layer. A coarse spatial resolution was chosen to examine how well the individual codes could simulate the large scale features using marginal resolution, and to force considerable energy into the sub-grid model in order to stretch the capabilities of the individual sub-grid models and differentiate between the various codes. They found similar performance across the codes with respect to the resolved field, with more marked differences between the sub-grid models. (Note that the terms sub-grid and sub-filter are more-or-less equivalent and are used often interchangeably). The work of Andren and his co-workers is used extensively in chapter 3 as a benchmark in validating the present work.

1.1.2   The Stable Regime   Stably stratified boundary layers are the least well suited for simulation with LES as the dominant structure size is quite small due to the damping of turbulent motion by the gravitational restoring force of a fluid who's density increases with height. While not ideal for LES, simulations of the stable case have been performed with reasonable results (Métais and Herring, 1989; Mason and Derbyshire, 1990; Coleman et al., 1992; Métais and Lesieur, 1992; Brown et al., 1994; Andren, 1995).

1.1.3   The Convective Regime   During daylight hours, when the net radiation to the Earth's surface is generally positive and sensible and latent heat is buoyantly transported up from the surface, we encounter typically the convective regime of the ABL. The turbulence structure of the convective boundary layer is marked by large coherent eddies that are of a size equivalent to the depth of the ABL (Garratt, 1992). We, therefore, have both the motivation and the justification for studying the convective regime with LES.

Deardorff (1970a, 1970b, 1972), using a finite-difference code, was the first to study ABL flows with LES. His simulations gave added support to the free convection theory that flow variables become independent of the friction velocity, u_*, under unstable stratification. The velocity fluctuations at heights above -L (the Obukhov Length) were shown to scale with w_*, the convective velocity scale. Furthermore, he showed that for even slightly unstable stratification the convection and turbulence extends up to the inversion base, suggesting that this height (z_i) is the most important scaling length and that $-z_i/L$ describes best the degree of

instability. He also examined the shape of the eddies, which provided insight into the profiles of mean quantities, and evaluated the effect of stability on the vertical travel time of particles released near the land surface (Deardorff, 1972).

Moeng (1984) drew on Deardorff's work and constructed a mixed pseudospectral - finite difference LES. She used this to simulate convective flow in the ABL and compared the simulation results to experimentally-derived data with reasonable success. Wyngaard and Brost (1984) used a finite-difference based LES and Moeng and Wyngaard (1984) used Moeng's LES to study the entrainment of scalars into the convective boundary layer and developed expressions for the eddy diffusivities of scalars for top-down and bottom-up transport. Holtslag and Moeng (1991) used the LES results of Moeng and Wyngaard (1989) to derive an improved countergradient term for bottom-up convective transfer and expressions for the eddy diffusivities. Holtslag and Moeng (1991) argued that the ratio of entrainment flux to surface flux is an important factor in defining the eddy diffusivities. Moeng and Wyngaard (1984) used LES to study vertical profiles of the variance of a scalar being transported from the land surface. This is relevant to surface fluxes in that under free convection conditions the scalar variance in the surface layer is directly related to the surface flux of the scalar (e.g. Albertson et al., 1995). Moeng and Wyngaard report that the LES-produced scalar variance agrees with experimental data in the mixed layer, but under-predicted the variance near the surface. They attribute this to the smaller scales being most active near the surface, causing much of the near-surface activity to occur in the sub-grid range of motions. This

is a weakness of LES and a focus of present improvement efforts (Mason, 1994). Similar problems exist with the ability of existing LES codes to represent physically reasonable values of the vertical velocity skewness near the surface (Moeng and Rotunno, 1990).

Hechtel et al. (1990) used Moeng's LES to study the effect of a nonhomogeneous temperature at the surface boundary on the first and second moments of the flow field in the *mixed layer*. They compared the case of a nonhomogeneous boundary to the homogeneous case, and found no noticeable effect on the moments in the outer region. On the contrary, Hadfield et al. (1991, 1992) found notable effects on the flow characteristics in the convective ABL from surface heat flux variations. They found persistent circulations with up-drafts over the high flux areas and down-drafts over the low flux areas. They also found stronger turbulence over the heat flux maxima. A mean horizontal wind was found to diminish the circulation and transport it downstream.

Sykes et al. (1993) used LES to study the structure of the surface layer. In particular they addressed the instantaneous friction velocity u_* resulting from large convective structures; the probability density function was examined and found to approach Gaussian and to be insensitive to surface roughness length. Their simulations depicted variations in the surface layer depth with surface roughness length.

Schumann (1989) used a finite-difference LES to study the turbulent transport of reactive and non-reactive species in the convective ABL and found both the

bottom-up and top-down diffusivities to depend on reaction rates and buoyancy. For the case without reaction, the bottom-up diffusivity was found to be twice as large as the top-down diffusivity because of buoyancy effects, as also noted by others. These results may be used to explore the conditions under which certain simple turbulence models, such as K-theory, may be employed. There is a body of literature emerging on the use of LES to study the dispersion of passive and reactive scalars in the ABL (e.g. van Haren and Nieuwstadt, 1989, 1990; Henn and Sykes, 1992; Mason, 1992; Nieuwstadt, 1992a, 1992b; Sykes et al., 1992; Sykes and Henn, 1992). These works have potential implications for modeling the transport of water vapor as well as pollutants and trace gases from the Earth's surface.

Schmidt and Schumann (1989) used Schumann's LES to study coherent structures in the unstable ABL. As large coherent convective structures are important flux mechanisms, their study may have direct implications for our understanding of the surface flux processes and the balances of water and energy at the Earth's surface. Schmidt and Schumann's results revealed that small scale plumes that are remote from the large scale convective plumes decay while rising through downdrafts rather than merging together. However, in the neighborhood of large thermals the smaller ones were sucked into the wake. The up-drafts and down-drafts together formed a spoke-like polygonal geometry – much like Rayleigh-Benard convection, yet less regular. They sought corroborative evidence from published field data, but their efforts were less than successful. They attributed this to insufficient spatial sampling in the field and, in part, to the potential ease with which these

patterns may be broken over inhomogeneous surfaces. Their results show entrainment flux at the inversion occurring through long wisps that are as long as the boundary layer is deep. Sorbjan (1995) has recently developed an LES code and applied it with a minimal number of nodes to study the growth of the convective boundary layer with constant surface flux of sensible heat.

Mason (1989) has also used LES to study the convective boundary layer and investigate the effect of the mesh resolution, the domain size, and the sub-grid model on the simulation results. The entrainment at the capping inversion displayed a distinct insensitivity to all three of these model characteristics. Mason reported a polygonal geometry of up-drafts similar to that of Schmidt and Schumann (1989). The downward entrainment of heat into the convective ABL at the inversion was resolved well by Mason's simulations, suggesting that this important process may be studied effectively by LES. He attributes the present success, in part, to an enhanced vertical mesh resolution near the inversion and suggests that future simulations, with say 128^3 grid points, hold promise for greater accuracy. The four LES codes of Moeng, Mason, Schumann, and Nieuwstadt have been compared for the convective case and reviewed by Nieuwstadt et al. (1991). These same codes have also been compared for the case of a neutrally stratified Ekman layer by Andren et al. (1994), with greater differences noted between the codes for simulating the neutral boundary layer than were seen here for the convective case.

1.1.4 Complex Terrain LES has been used to study the effect of a wavy land surface on turbulent convection in the boundary layer (e.g. Krettenauer and Schu-

mann, 1992; Walko et al., 1992; Schumann, 1993; Dornbrack and Schumann, 1993). Schumann (1993) concluded that terrain-induced coherent structures are only produced when the amplitude of the terrain undulation is large with respect to the depth of the boundary layer. He also showed the wavy terrain to have a minimal effect on the length scales for vertical velocity and vertical velocity variance, a statistic known to be important to scalar transport from the land surface (e.g. Katul et al., 1994). Walko et al. (1992) also studied the effect of hilly terrain on the convective ABL (200 m hills in 1 km deep boundary layer), but they found noticeable effects on certain flow measures. Interestingly, Walko et al. found the horizontally averaged statistics of flow over hilly terrain to be similar to those obtained over flat terrain; however, they found significant effects in the spectra and also found pronounced amounts of sub-grid turbulent kinetic energy and vertical heat flux above the higher terrain. These results, when considered along with those from field investigations over similar terrain (e.g. Kustas and Brutsaert, 1986), may lend insight into the effect of non-ideal terrain on simple turbulence models that are based on homogeneity assumptions. The turbulent structure of up-slope boundary layers is also being investigated with LES (e.g. Schumann, 1990).

In a unique study, Shaw and Schumann (1992) simulated the atmospheric surface layer above and within a forest. Their flow domain only extended three forest heights in the vertical and, therefore, did not encompass the entire depth of the ABL. This limited vertical extent is charged with causing some departure of the simulation results from field experimental evidence. However, they did capture

features noted in field data. Perhaps most important about this study is that it opened to LES the modeling of the ABL over forested landscape. Extensions of this work using larger flow domains could leverage the results of field experience over complex forest terrain (e.g. Brutsaert and Parlange, 1992; Parlange and Brutsaert, 1993) toward an improved understanding of regional scale surface fluxes.

1.2 Land-Atmosphere Scale Interaction and LES

The majority of LES applications to the ABL have included homogeneous surface conditions and have been designed to study the structure of turbulence in the boundary layer well away from the wall. However, for the few cases with inhomogeneous surface conditions, some effect on the turbulence structure has often been noted (e.g. Hadfield et al., 1991, 1992; Walko et al., 1992; Shen and Leclerc, 1995). In this study we seek to identify the dependence of the aggregate flux across the land-atmosphere interface on the spatial scale of surface patches. From the above review it is clear that LES is capable of simulating accurately the neutral and unstable ABL. With this motivation we proceed to develop, validate, and apply a new LES code to the present problem.

The following chapter describes the mathematical foundation of the large eddy simulation code and the numerical techniques used to implement the governing equations.

CHAPTER 2

Theoretical Framework and Implementation

In this chapter the basic equations of motion and transport are manipulated
to form the set of equations for the large eddy simulation (LES) technique. These
equations are then further manipulated to a form tailored for the specific applica-
tions envisioned for the present code. Finally, the equations are treated numeri-
cally for code implementation, and the general solution algorithm is outlined. The
actual Fortran source code is attached as Appendix C.

2.1   General LES Equations

For additional background on the basic equation development see McComb
(1990, pp. 118-124) and the collection of papers in Galperin and Orszag (1993).

2.1.1   <u>Velocity</u> For an incompressible fluid the conservation of mass is represented
by

$$\partial_i U_i = 0 \tag{2.1}$$

and the conservation of momentum per unit mass by

$$\partial_o U_i + U_j \partial_j U_i = -\frac{1}{\rho}\partial_i P + \nu \partial_j \partial_j U_i - g\delta_{i3} \tag{2.2}$$

where, δ_{ij} ($1 \; for \; i = j$; $0 \; for \; i \neq j$) is the Kronecker delta, ∂_o is the par-
tial derivative operator with respect to time, U_i is the instantaneous velocity in
the x_i direction, ∂_i is the partial derivative operator with respect to the x_i direction

(i.e. $\frac{\partial}{\partial x_i}$), P is the pressure, ν is the kinematic viscosity, g is the acceleration due to gravity, the coordinate system is Cartesian ($x_1 = x$, $x_2 = y$, $x_3 = z$), with z being normal to the wall and x being along the mean wind direction, and summation is implied on all repeated subscripts (i.e. $\partial_j \partial_j U_i = \partial_1 \partial_1 U_i + \partial_2 \partial_2 U_i + \partial_3 \partial_3 U_i$). For a review of the tensor notation see Panton (1984, Ch. 3). Note that Coriolis effects have been neglected, as our focus is on surface layer turbulence which is generally insensitive to the Earth's rotation (e.g. Kaimal and Finnigan, 1994).

Boussinesq Approximation   For simplicity the mean hydrostatic balance ($\partial_3 \langle P \rangle +$ $\langle \rho \rangle g = 0$) is subtracted from the vertical momentum equation, so that the resulting equation only represents departures from this balance. Following several simple steps (see Stull, 1988, pp.83-85) the momentum equation (2.2) becomes

$$\partial_o U_i + U_j \partial_j U_i = -\frac{1}{\rho_o} \partial_i P'' + \nu \partial_j \partial_j U_i - \frac{\rho''}{\rho_o} g \delta_{i3} \qquad (2.3)$$

where ρ_o is the hydrostatic density, ρ'' represents fluctuations from this equilibrium value (note in practice that $\frac{\rho''}{\rho_o}$ is replaced by $\frac{-\theta''}{\theta_o}$), θ is potential temperature, θ_o is the reference potential temperature, $\langle . \rangle$ represents the horizontal averaging operator, and the double prime ($''$) represents departures from the hydrostatic equilibrium value (e.g. $P'' = P- < P >$). Note in this form gravity acts only on the perturbation from hydrostatic. Throughout this work we will use the form in terms of temperature fluctuations rather than explicitly simulating density, viz.

$$\partial_o U_i + U_j \partial_j U_i = -\frac{1}{\rho_o}\partial_i P'' + \nu \partial_j \partial_j U_i + \frac{\theta''}{\theta_o}g\delta_{i3} \qquad (2.4)$$

where, of course, positive temperature fluctuations tend to induce an upward acceleration (buoyant motion).

Filtering As mentioned in Chapter 1, flows in the ABL possess excessive degrees of freedom for direct simulation. Therefore, with the LES technique the individual velocity and scalar fields are explicitly decomposed into resolved and unresolved fields. This is somewhat analogous to the Reynolds averaging technique, where fields are decomposed into a mean field and a fluctuation field. However, here the resolved field contains the mean and the large scale portions of the fluctuation field, while the unresolved field contains only the small scale fluctuations. See Leonard (1974) and Aldama (1990) for a full account of the filtering and its effects.

The flow variables are filtered by the explicit application of a general filter G to define the resolved field

$$\bar{u}_i(x_1, x_2, x_3) = \oint U_i(x_1', x_2', x_3') G(x_1 - x_1', x_2 - x_2', x_3 - x_3') dx_1' dx_2' dx_3' \qquad (2.5)$$

such that the total instantaneous value may be represented as the sum of filtered and sub-grid components

$$U_i = \bar{u}_i + u_i' \qquad (2.6)$$

where $\bar{u}_i$ is the resolved portion of the x_i direction velocity and u_i' is the sub-grid or unresolved portion. Both $\bar{u}_i$ and u_i' vary in time and space. We should note that for the case of a general filter $\bar{\bar{u}}_i$ does not necessarily equal $\bar{u}_i$, in contrast

to Reynolds averaging rules (see Aldama, 1993). Consequently, terms such as $\overline{\bar{u}_j u'_i}$ do not generally vanish. We restrict consideration to homogeneous filters, i.e. $G(x_1 - x'_1, x_2 - x'_2, x_3 - x'_3) = G(\Delta x_1, \Delta x_2, \Delta x_3)$, such that the filtering process commutes with differentiation.

The filtering operation is applied to (2.1) to obtain the continuity equation for the resolved (filtered) field

$$\partial_i \bar{u}_i = 0 \tag{2.7}$$

where we have made use of the commutativity of the filtering and differentiation operators for homogeneous filters. In a similar manner we obtain the momentum equation for the filtered field

$$\partial_o \bar{u}_i + \partial_j \overline{\bar{u}_i \bar{u}_j} = -\frac{1}{\rho_o} \partial_i \bar{p}'' + \nu \partial_j \partial_j \bar{u}_i - \partial_j R_{ij} + \bar{\beta} \delta_{i3} \tag{2.8}$$

where a buoyancy term $\bar{\beta}$ is introduced to represent $\frac{\overline{\theta''}}{\theta_o} g$, and through use of (2.7), we have replaced $\overline{\bar{u}_j \partial_j \bar{u}_i}$ with $\partial_j \overline{\bar{u}_i \bar{u}_j}$. Here the Leonard stress term $\overline{\bar{u}_i \bar{u}_j} - \bar{u}_i \bar{u}_j$ is being treated explicitly through application of the filter to the product of filtered velocities, and the total sub-grid (i.e. sub-filter) stress tensor is represented as

$$R_{ij} = \overline{\bar{u}_i u'_j} + \overline{u'_i \bar{u}_j} + \overline{u'_i u'_j} \tag{2.9}$$

Note the closure problem, as the momentum equation for the resolved field (2.8) contains unresolved terms (i.e. R_{ij}). The set (2.7), (2.8) and (2.9) form the general set of LES equations of motion, with (2.9) requiring closure attention. Following an introduction to the scalar transport equations, we depart from the general and perform additional manipulation to tailor the equations to the present approach.

<u>2.1.2 Scalars</u> The LES described here simulates the transport of two scalars, potential temperature (θ) and water vapor (q), but can easily be adapted to handle other scalars (whether passive, active, or reactive). For a description of potential temperature and its relationship to "regular temperature" see Brutsaert (1982, pp. 44-45). To minimize redundancy we consider the transport of a general passive, non-reactive scalar S, represented by the transport equation

$$\partial_o S + U_j \partial_j S = D^s \partial_j \partial_j S \qquad (2.10)$$

where D^s is a constant molecular diffusivity of scalar S in air.

As with velocity, the resolved scalar field is defined through a filtering operation (i.e. (2.5)). With this filter applied to (2.10), transport of the resolved scalar field is represented by

$$\partial_o \bar{s} + \overline{u_j \partial_j \bar{s}} = D^s \partial_j \partial_j \bar{s} - \partial_j \pi_j^s \qquad (2.11)$$

with the sub grid flux of S represented by

$$\pi_j^s = \overline{\bar{u}_j s'} + \overline{u_j' \bar{s}} + \overline{u_j' s'} \qquad (2.12)$$

This leaves a closure problem for the scalar transport analogous to that for the velocity.

2.2 Further Manipulation of the LES Equations

2.2.1 Velocity It is convenient to remove the trace from R_{ij} and add it to the

pressure

$$\tau_{ij} = R_{ij} - \frac{1}{3}R_{kk}\delta_{ij} \qquad (2.13)$$

$$\overline{p^1} = \frac{\bar{p}''}{\rho_o} - \frac{1}{3}R_{kk} \qquad (2.14)$$

The momentum equation (2.8) is revised

$$\partial_o \bar{u}_i + \partial_j \overline{u_i u_j} = -\partial_i \overline{p^1} + \nu \partial_j \partial_j \bar{u}_i - \partial_j \tau_{ij} + \bar{\beta}\delta_{i3} \qquad (2.15)$$

For pointwise energy conservation, in addition to momentum conservation, we

replace the convective term with its rotational form using the incompressible flow

identity (Orszag and Pao, 1974; Ferzinger and Perić, 1996, p. 156)

$$\partial_j \overline{u_i u_j} = \overline{u_j(\partial_j \bar{u}_i - \partial_i \bar{u}_j)} + \frac{1}{2}\partial_i \overline{u_j u_j} \qquad (2.16)$$

The gradient of resolved kinetic energy is combined with the pressure gradient,

such that the momentum equation becomes

$$\partial_o \bar{u}_i + \overline{u_j(\partial_j \bar{u}_i - \partial_i \bar{u}_j)} = -\partial_i \overline{p^0} + \nu \partial_j \partial_j \bar{u}_i - \partial_j \tau_{ij} + \bar{\beta}\delta_{i3} \qquad (2.17)$$

where the new pressure term is

$$\overline{p^0} = \overline{p^1} + \frac{1}{2}\overline{u_j u_j} = \frac{\bar{p}''}{\rho_o} - \frac{1}{3}R_{kk} + \frac{1}{2}\overline{u_j u_j} \qquad (2.18)$$

The equations are non-dimensionalized by a global boundary layer length scale

z_s (e.g. depth of ABL or height of capping inversion) and the friction velocity u_*,

such that the continuity equation becomes

$$\widehat{\partial}_i \widehat{\bar{u}}_i = 0 \qquad (2.19)$$

and the momentum equation becomes

$$\widehat{\partial}_o \widehat{\bar{u}}_i + \overline{\widehat{\bar{u}}_j(\widehat{\partial}_j \widehat{\bar{u}}_i - \widehat{\partial}_i \widehat{\bar{u}}_j)} = -\widehat{\partial}_i \widehat{\overline{p^o}} + \frac{1}{R_{e_\tau}} \widehat{\partial}_j \widehat{\partial}_j \widehat{\bar{u}}_i - \widehat{\partial}_j \widehat{\tau}_{ij} + \widehat{\beta} \delta_{i3} \qquad (2.20)$$

We are using $\widehat{()}$ temporarily to make the point that these variables and operators are non-dimensional and to distinguish them from those used above (e.g. $\widehat{\bar{u}}_i = \bar{u}_i/u_*$; $\widehat{x} = x/z_s$; $\widehat{t} = t u_*/z_s$, $\widehat{\partial}_j = z_s \partial_j$). As we envision z_s to be $\bigcirc(1000m)$, and u_* to be $\bigcirc(1\ m/s)$, $\frac{1}{R_{e_\tau}}$ is about 10^{-8}. Therefore, we omit the viscous term $\left(\frac{1}{R_{e_\tau}} \widehat{\partial}_j \widehat{\partial}_j \widehat{\bar{u}}_i\right)$ from consideration as it is many orders of magnitude smaller than the inertial terms. Since the combination of $\widehat{()}$ and $\overline{()}$ is cumbersome, we return to the non-hat form with the understanding that all variables are nondimensional from here forward. Furthermore, we break a constant mean streamwise pressure gradient, F_p, out of the total pressure gradient term to identify the driving force in the flow (i.e. pressure driven boundary layer flow, $\left\langle \frac{dP}{dx} \right\rangle = const.$). This yields the equations of large scale motion in their final form before numerical treatment and closure

$$\partial_i \bar{u}_i = 0 \qquad (2.21)$$

and

$$\partial_o \bar{u}_i + \overline{\bar{u}_j(\partial_j \bar{u}_i - \partial_i \bar{u}_j)} = -\partial_i \bar{p} + F_p \delta_{i1} - \partial_j \tau_{ij} + \beta \delta_{i3} \qquad (2.22)$$

For simplicity $\bar{p}$ is being written in place of $\overline{p^0} - F_p x_1$. The closure model is introduced next.

Sub Grid Stress (SGS) Model for Velocity   For closure of (2.22) it is necessary

to obtain an expression for τ_{ij} in terms of the resolved fields. In the present code

we use the simple eddy viscosity model for the sub-grid stress (after Smagorinsky,

1963)

$$\tau_{ij} = -2\nu_T \bar{S}_{ij} \qquad (2.23)$$

where

$$\bar{S}_{ij} = \frac{1}{2}(\partial_j \bar{u}_i + \partial_i \bar{u}_j) \qquad (2.24)$$

A turbulent (eddy) viscosity is formulated from Prandtl's mixing length model

$$\nu_T = C_1 q l \qquad (2.25)$$

where q is an appropriate velocity scale and l an appropriate length scale, repre-

sentative of the length scale at which energy is passed from the resolved to the

sub-grid field (i.e. l is related to the filter width). Equating the production of SGS

kinetic energy

$$\wp = 2\nu_T \bar{S}_{ij} \bar{S}_{ij} \qquad (2.26)$$

with a Kolmogorov-like estimate of the dissipation ($Diss. = q^3/l$) yields Smagorin-

sky's (1963) model for the eddy viscosity

$$\nu_T = C_1 q l = (C_s l)^2 \sqrt{2\bar{S}_{ij}\bar{S}_{ij}} \qquad (2.27)$$

$$\tau_{ij} = -2\left[(C_s l)^2 \sqrt{2\bar{S}_{ij}\bar{S}_{ij}}\right]\bar{S}_{ij} \qquad (2.28)$$

Smagorinsky's constant C_s has some tie (Lilly, 1966) to the Kolmogorov constant

from inertial subrange theory, but is most often taken as a free parameter with

typical values around 0.2. The Smagorinsky model has proven adequate away from

walls, but requires amendment near solid boundaries (Moin et al., 1978). Other workers (e.g. Moeng, 1984) deduce an eddy viscosity from a prognostic equation for the sub-grid TKE. The attractive nature of the TKE equation is that it also yields estimates of the sub-grid TKE as necessary to back a physical pressure value and sub-grid velocity variances out of the composite term that is loosely referred to as pressure in this work. Yet other workers have proposed models that allow for backscatter of energy from the sub-grid to the resolved scales (e.g. Mason and Thompson, 1992), where the proportion of energy backscaterred up the spectrum is estimated through the Eddy-Damped Quasi-Normal Markovian (EDQNM) theory. However, we employ the Smagorinsky model for its simplicity and typically acceptable performance.

Near the wall we wish to match this model (2.28) to a form that asymptotes to the ensemble wall model discussed below in the boundary conditions section. Mason (1994) suggests the following model for application near the wall

$$\nu_T = k^2(z + z_o)^2 \partial_3 U_r \tag{2.29}$$

where $k(= 0.4)$ is the von Karman constant, $U_r(= (\overline{u}_1^2(z) + \overline{u}_2^2(z))^{\frac{1}{2}})$ is the resultant horizontal wind speed at height z, and z_o is the local surface roughness length. This model is basically identical to Smagorinsky's with the length scale set to $k(z + z_o)$, since $\partial_3 U_r$ is the dominant velocity gradient near the wall. This can be implemented by using (2.27) with an interpolating length scale such as

$$l^{-n} = \{k(z + z_o)\}^{-n} + l_m^{-n} \tag{2.30}$$

where l is the length scale to be used in the SGS model for smooth transition, n is

an arbitrary interpolation parameter, and l_m is the predefined length scale (original Smagorinsky model) that represents the grid spacing in the internal portion of the domain (Mason, 1994). Note that as z becomes much greater than l_m, l approaches l_m. Here we use (2.30) in (2.28) with n=3. Figure 2.1 shows how l scales with distance from the wall for a case with $l_m = 38\ m$.

2.2.2 Scalars

The scalar transport equations are non-dimensionalized by the friction velocity u_*, the global boundary layer length scale z_s, and some general scalar scale, such as $S_*(= \frac{\pi_3^s}{u_*})$, to arrive at

$$\hat{\partial}_o \hat{\bar{s}} + \overline{\hat{u}_j \hat{\partial}_j \hat{\bar{s}}} = \frac{D^s}{u_* z_s} \hat{\partial}_j \hat{\partial}_j \hat{\bar{s}} - \hat{\partial}_j \hat{\pi}_j^s \tag{2.31}$$

where

$$\frac{D^s}{u_* z_s} = \frac{D^s}{\nu R_\tau} = O(\frac{1}{R_\tau}) = O(10^{-8}) \tag{2.32}$$

Therefore, we can neglect the molecular diffusion of the scalar relative to the turbulent flux. And, as for the velocity, we drop the (^) notation and keep in mind that from hereon the equations are dimensionless. With these modifications (2.31) becomes

$$\partial_o \bar{s} + \overline{\bar{u}_j \partial_j \bar{s}} = -\partial_j \pi_j^s \tag{2.33}$$

Sub Grid Stress (SGS) Model for Scalars

In keeping with the simple Smagorinsky (1963) model, we employ an eddy diffusivity model for the sub-grid scalar flux
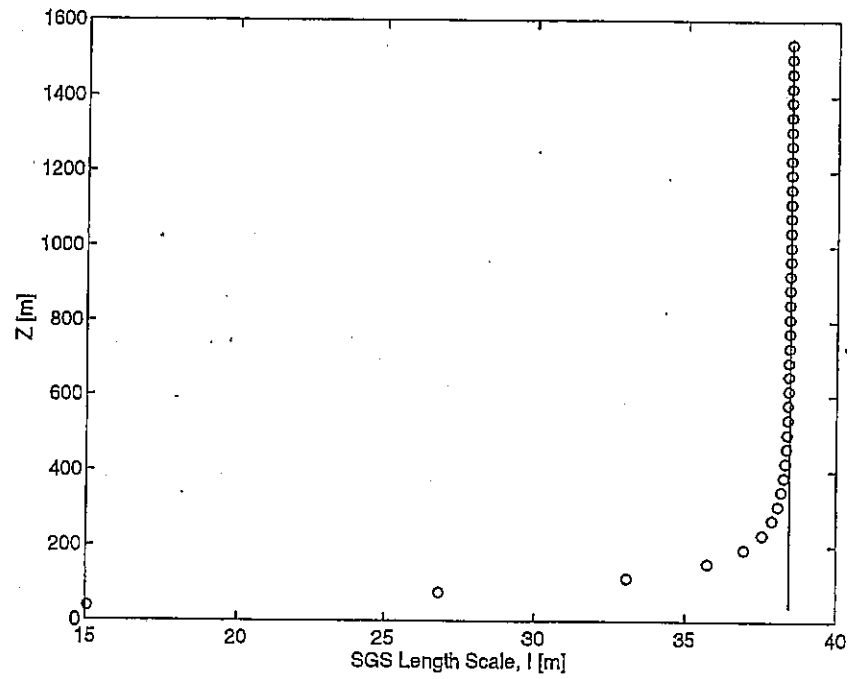
Figure 2.1: Sub-grid model length scale versus height above the wall. The vertical line denotes the mesh spacing l_m and the circles are the interpolation length scale with n=3.

$$\pi_j^s = -D_T^s \partial_j \bar{s} \tag{2.34}$$

where, as with most LES (e.g. Andren et al., 1994), the turbulent diffusivity is related to the turbulent (eddy) viscosity by a Schmidt number

$$D_T^s = \frac{\nu_T}{S_c} \tag{2.35}$$

with S_c being $\bigcirc(1)$.

2.2.3 Final Set of Analytic Equations

Before addressing numerical treatment, we list together for future reference the set of analytic equations describing motion and transport in this LES code

$$\partial_o \bar{u}_i + \overline{\bar{u}_j(\partial_j \bar{u}_i - \partial_i \bar{u}_j)} = -\partial_i \bar{p} + F_p \delta_{i1} - \partial_j \tau_{ij} + \beta \delta_{i3} \tag{2.36}$$

$$\partial_o \bar{\theta} + \overline{\bar{u}_j \partial_j \bar{\theta}} = -\partial_j \pi_j^\theta \tag{2.37}$$

$$\partial_o \bar{q} + \overline{\bar{u}_j \partial_j \bar{q}} = -\partial_j \pi_j^q \tag{2.38}$$

supplemented by (i) the continuity equation, which will be used later to derive an equation to deduce the pressure field from the velocity field,

$$\partial_i \bar{u}_i = 0 \tag{2.39}$$

(ii) closure equations for the sub-grid fluxes

$$\tau_{ij} = -2\nu_T \bar{S}_{ij} \tag{2.40}$$

$$\pi_j^\theta = -\frac{\nu_T}{S_c} \partial_j \bar{\theta} \tag{2.41}$$

$$\pi_j^q = -\frac{\nu_T}{S_c}\partial_j\bar{q}$$

(2.42)

and (iii) the sub-grid viscosity form

$$\nu_T = C_1 q l = (C_s l)^2 \sqrt{2\bar{S}_{ij}\bar{S}_{ij}}$$

(2.43)

Therefore, we have three momentum equations for the three velocity components, a continuity equation for the pressure, two transport equations for the two scalars, nine sub-grid momentum flux closure equations for the nine sub-grid momentum fluxes, and six sub-grid scalar flux closure equations for the six sub-grid scalar fluxes(2 scalars x 3 directions). Hence, the system is closed, pending adequate prescription of boundary and initial conditions.

2.2.4   Boundary Conditions The horizontal directions are assigned periodic boundary conditions, such that for any primitive flow variable, A, we have

$$A(x + mL_x, y + nL_y, z) = A(x, y, z)$$

(2.44)

where L_x and L_y are the domain dimensions in the x and y direction, and m and n are signed integers. This condition is a great help in turbulence simulation because it is necessary to have fully developed turbulence on both the inflow and exit faces of the domain. However, it is important to prescribe a domain size that is physically large enough to ensure that the flow becomes completely uncorrelated as it passes across the domain (L_x) from inlet to exit. Typically, the domain length is kept larger than twice the lag value at which the velocity autocorrelation function vanishes. With the present applications this criterion is well exceeded, as the domain length is at least 2 km.

The top boundary is positioned well above the top of the boundary layer and assigned a condition of vanishing vertical gradients (no stress) and no flow through the boundary, such that

$$\partial_3 \bar{u}_i = \partial_3 \bar{\theta} = \partial_3 \bar{q} = \bar{u}_3 = 0; \quad at \ z = top \qquad (2.45)$$

The bottom boundary is far more critical to the structure of the turbulence than the sides and top. This is because the mechanical turbulence is produced as a result of drag at the wall, and the heat flux responsible for the convective motion is introduced at the wall as well. The exchange of scalars and momentum between the flow and the surface are affected by exchange equations that depend on the properties of the surface and the instantaneous properties of the resolved flow in the immediate neighborhood of the surface.

The surface shear stress is computed over the bottom boundary as a function of local roughness length (z_o) and near surface resolved velocity by integrating the logarithmic velocity gradient from $z = z_o$ to the height of the first node above the wall, to obtain

$$\tau_w = -\left[\frac{U_r k}{\ln(z/z_o)} \right]^2 \qquad (2.46)$$

where U_r is the resultant resolved velocity $[(\bar{u}_1^2 + \bar{u}_2^2)^{\frac{1}{2}}]$ at height z. This approach ignores the effect of density stratification on the velocity gradient over the first grid interval above the wall – an effect that could be easily accounted for by application of Monin-Obukhov similarity theory as described in Brutsaert (1982). This wall function is the near-wall limit of the SGS model described above. It is attractive since the longitudinal momentum is forced by vertical gradients in the horizontal

shear stress, and we want to avoid spurious gradients arising from abrupt changes in the shear stress (SGS) model. We then follow Schmidt and Schumann (1989) to partition the stress as

$$\tau_{i,3}\big|_{wall} = \tau_w \left[\frac{\bar{u}_i(z)}{U_r(z)} \right], \qquad i = 1, 2 \tag{2.47}$$

While it is understood that this type of wall function has its roots as a relationship between mean values, it has been extended to instantaneous values in boundary layer simulations in the past (e.g. Moeng, 1984; Mason and Callen, 1986; Schmidt and Schumann, 1989). We envision its use as a wall-specific sub grid model which relates instantaneous resolved velocity fields to local instantaneous shear stress. The shear stress at the interior nodes will be computed by the eddy viscosity model, and the divergence of the shear stresses will work on the resolved velocities by way of the momentum equations. The refined wall function boundary conditions described by Piomelli et al. (1989), which may be more physically-based than the use of "mean" transfer functions for the instantaneous fields, require a horizontally homogeneous roughness length for implementation and are, therefore, not directly applicable to the present applications of flow over heterogeneous surfaces.

Because the mesh is staggered (described fully below), with vertical velocity values assigned to nodes located vertically offset from the longitudinal and transverse velocity nodes, we do not have simple no-slip boundary conditions for the x- and y-direction velocities. The vertical velocity boundary condition is simply

$$\bar{u}_3 = 0; \quad at \ z = 0 \tag{2.48}$$

The longitudinal and transverse velocities begin at $\frac{\Delta z}{2}$ above the wall. Therefore, $\bar{u}_1$ and $\bar{u}_2$ do no receive formal no-slip boundary conditions. This is common for LES as the motion is not resolved completely to the wall. One complication is that values of the vertical gradients of $\bar{u}_1$ and $\bar{u}_2$ are needed at the first position above the wall ($z \doteq \Delta z/2$) for the convective term and the SGS stress calculation. Moeng (1984) calculated these gradients from the computed instantaneous shear stress at the wall node and an assumed logarithmic velocity profile, viz.

$$\partial_3 \bar{u}_i(x, y, \frac{\Delta z}{2}) = \frac{(-\tau_{i,3}(x, y, o))^{\frac{1}{2}}}{k \frac{\Delta z}{2}} \tag{2.49}$$

However, this relationship can exhibit undesired behavior, such as creating a negative correlation between $\partial_3 \bar{u}_1$ and $\bar{u}_3$ at $\frac{\Delta z}{2}$ which serves to accelerate the mean flow just above the wall. To see where the negative correlation results from, we note that for a net downward momentum flux an instantaneous $+\Delta \bar{u}_1$ implies a $-\Delta \bar{u}_3$, and we track a $+\Delta \bar{u}_1$ through (2.46) to create a $-\Delta \tau_{13}$, which from (2.49) yields a $+\Delta \partial_3 \bar{u}_1$ – hence a negative correlation between $\partial_3 \bar{u}_1$ and $\bar{u}_3$, which serves to (erroneously) accelerate the flow at this position $z = \frac{\Delta z}{2}$. To avoid this a different means of computing $\partial_3 \bar{u}_i$ at $\frac{\Delta z}{2}$ is proposed. First, we make use of the acceptable performance of the (2.49) relationship in relating mean surface stress to mean velocity gradients and compute

$$< \partial_3 \bar{u}_i(\frac{\Delta z}{2}) > = \frac{(< -\tau_{i,3}(z = o) >)^{\frac{1}{2}}}{k \frac{\Delta z}{2}} \tag{2.50}$$

then a forward differencing of the portion of the $\bar{u}_i$ field that departs from the mean field

$$\left\{\partial_3\bar{u}_i(x,y,\frac{\Delta z}{2})\right\}' = \frac{\left(\bar{u}_i(x,y,\frac{3\Delta z}{2}) - <\bar{u}_i(\frac{3\Delta z}{2})>\right) - \left(\bar{u}_i(x,y,\frac{\Delta z}{2}) - <\bar{u}_i(\frac{\Delta z}{2})>\right)}{\Delta z}$$

(2.51)

is added to the mean gradient to form an approximation of the local instantaneous gradient.

$$\partial_3\bar{u}_i(x,y,\frac{\Delta z}{2}) = <\partial_3\bar{u}_i(\frac{\Delta z}{2})> + \left\{\partial_3\bar{u}_i(x,y,\frac{\Delta z}{2})\right\}'$$

(2.52)

This approach (implemented in the subroutine "derivwall" attached in Appendix C) yields clearly improved results over (2.49) in test runs of the LES code.

The scalars have specified finite values on the surface, i.e. $q(x,y,0)$ *and* $\theta(x,y,0)$, which in combination with instantaneous values in the near surface region of the flow define the vertical scalar flux at the wall through

$$\pi_3^\theta(x,y,0) = \frac{\left(\bar{\theta}(x,y,0) - \theta(x,y,\frac{\Delta z}{2})\right)k(-\tau_w)^{\frac{1}{2}}}{\ln(\frac{\Delta z/2}{z_{oh}})}$$

(2.53)

$$\pi_3^q(x,y,0) = \frac{\left(\bar{q}(x,y,0) - q(x,y,\frac{\Delta z}{2})\right)k(-\tau_w)^{\frac{1}{2}}}{\ln(\frac{\Delta z/2}{z_{ov}})}$$

(2.54)

where $(-\tau_w)^{\frac{1}{2}}$ is the local friction velocity, and z_{oh} and z_{ov} are the scalar surface roughness lengths for heat and water vapor, respectively. (taken as simple functions of z_o.) The vertical scalar gradients at $\frac{\Delta z}{2}$ are computed, as with the velocity, using mean gradients from a log-law

$$< \partial_3\bar{\theta}(\frac{\Delta z}{2}) > = \frac{< -\pi_3^\theta(z=0) >}{< (-\tau_w) >^{\frac{1}{2}} k\frac{\Delta z}{2}}$$

(2.55)

$$< \partial_3\bar{q}(\frac{\Delta z}{2}) > = \frac{< -\pi_3^q(z=0) >}{< (-\tau_w) >^{\frac{1}{2}} k\frac{\Delta z}{2}}$$

(2.56)

with local perturbation gradients

$$\left\{\partial_3\bar\theta(x,y,\frac{\Delta z}{2})\right\}' = \frac{\left(\bar\theta(x,y,\frac{3\Delta z}{2})- <\bar\theta(\frac{3\Delta z}{2})>\right) - \left(\bar\theta(x,y,\frac{\Delta z}{2})- <\bar\theta(\frac{\Delta z}{2})>\right)}{\Delta z}$$

(2.57)

$$\left\{\partial_3\bar q(x,y,\frac{\Delta z}{2})\right\}' = \frac{\left(\bar q(x,y,\frac{3\Delta z}{2})- <\bar q(\frac{3\Delta z}{2})>\right) - \left(\bar q(x,y,\frac{\Delta z}{2})- <\bar q(\frac{\Delta z}{2})>\right)}{\Delta z}$$

(2.58)

to form total, instantaneous, local gradients

$$\partial_3\bar\theta(x,y,\frac{\Delta z}{2}) = <\partial_3\bar\theta(\frac{\Delta z}{2})> + \left\{\partial_3\bar\theta(x,y,\frac{\Delta z}{2})\right\}' \qquad (2.59)$$

$$\partial_3\bar q(x,y,\frac{\Delta z}{2}) = <\partial_3\bar q(\frac{\Delta z}{2})> + \left\{\partial_3\bar q(x,y,\frac{\Delta z}{2})\right\}' \qquad (2.60)$$

The pressure field receives periodic horizontal boundary conditions and verti-
cal boundary conditions from considerations of the vertical momentum equation
written at the wall and the top of the domain. The details are shown later in
the derivation of the pressure solution, as the specific numerical treatment of the
fields is of central importance to deriving the solution equation for computing the
pressure.

2.3   Numerical Treatment

With periodic boundary conditions in the x and y directions the flow vari-
able fields may be transformed horizontally into periodic functions for numerical
treatment. The vertical direction is not periodic and must be treated either with
special transform techniques (e.g. Chebyshev polynomials) or with more classical
numerical techniques such as finite difference. In the present LES code the nu-
merics are mixed, with a Fourier-based pseudospectral approach in the horizontal

directions and finite difference in the vertical (after Moin et al., 1978). Through this section descriptions will be given of the computational domain, the discrete transform, pseudospectral differentiation, the spatial finite differencing details, the finite difference time integration, the discrete solution of the pressure field from the velocity field, and the solution algorithm which implements all of the above steps toward the integration of the equations of motion and transport in space and time.

2.3.1 <u>Computational Domain</u> The numerical simulation is of turbulent flow in the ABL, and as the largest eddies fill the boundary layer depth (e.g. Schmidt and Schuman, 1989 for the convective case), the flow domain must cover at least the full depth of the ABL ($\approx$ 1-2 km). In this work the top boundary is defined to be some factor times the boundary layer scaling length, i.e. $L_z = \eta z_s$, where $\eta \geq 1$. The horizontal extent of the domain must be large enough to cover the surface of interest and must be significantly greater than the correlation length of the turbulence. To simplify the explanation and implementation of the spectral numerics the horizontal directions have been chosen to be fixed at $2\pi z_s$; with slight modification to the code surrounding the Fourier transform routine this constraint can be relaxed. Hence, the actual physical dimensions of the domain will vary with the boundary layer depth for individual applications, or runs, of the code. For generality, we begin by referring to the domain dimensions in the longitudinal (x), transverse (y), and vertical (z) directions as L_x, L_y, and L_z, respectively. See Figure 2.2 for a sketch of the simulation domain and the alignment of the
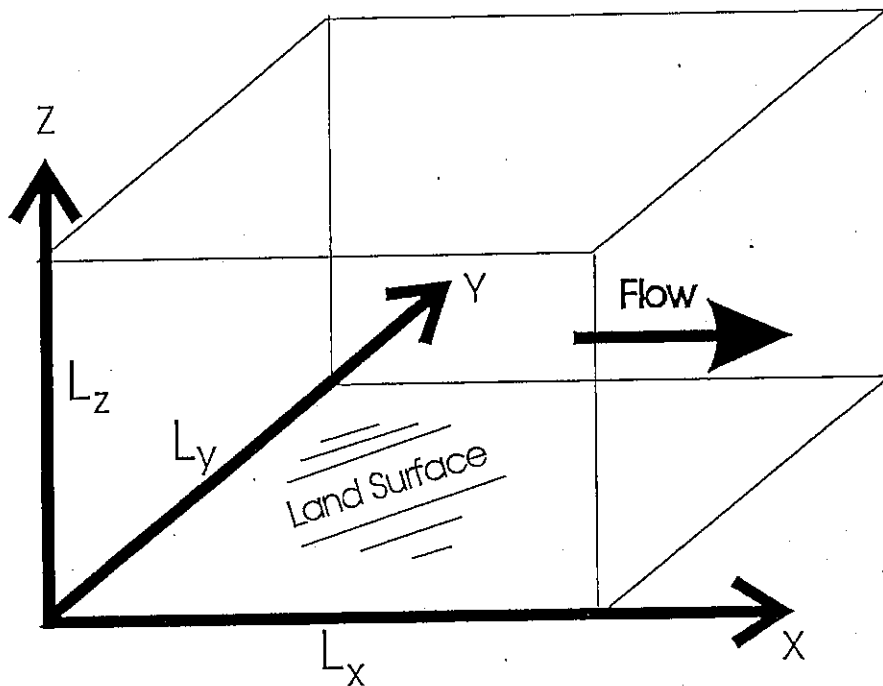
coordinate directions relative to the flow.

Figure 2.2: Atmospheric boundary layer simulation domain. L_x is the domain extent in the streamwise direction, L_y the extent in the spanwise direction, and L_z the extent in the vertical direction.

The continuous fields are represented by a discrete mesh with N_x nodes in the x-direction, N_y nodes in the y-direction, and N_z nodes in the z-direction. Hence, the domain volume $L_x L_y L_z$ is covered by a total of $N_x N_y N_z$ nodes. In its present form the LES employs uniform grid spacing in each the x, y, and z directions, such that the dimensional grid-spacing is defined as

$$^d\triangle x = \frac{L_x}{N_x}; \quad ^d\triangle y = \frac{L_y}{N_y}; \quad ^d\triangle z = \frac{L_z}{N_z - 1} \tag{2.61}$$

where the superscript is just to denote dimensional. As described above, the com-

putations are dimensionless, with the distances non-dimensionalized by a global boundary layer length scale, z_s. As $L_x = 2\pi z_s$, $L_y = 2\pi z_i$, and $L_z = \eta z_s$, we have dimensionless grid spacing of

$$\Delta x = \frac{2\pi}{N_x}; \quad \Delta y = \frac{2\pi}{N_y}; \quad \Delta z = \frac{\eta}{N_z - 1}. \quad (2.62)$$

The horizontal directions are periodic with the last node considered implicitly to be the same as the first. So in considering N_x unique nodes, we have N_x internode spaces, or "elements", yet in the vertical direction N_z nodes relate to only $N_z - 1$ internode spaces. See Figure 2.3 for a sketch of the relation between the number of nodes and the mesh spacing. Another restriction of the present implementation is that N_x and N_y must be positive integer powers of 2 (e.g. 32, 64, 128, or 256). With a minor modification of the Fast Fourier Transform (FFT) algorithm this restriction could be relaxed. There is no such limitation on N_z.

The mesh is staggered in the vertical, with the vertical velocity ($\overline{u}_3 = \overline{w}$) stored halfway between the other variables. A detailed explanation for this is given below in the course of deriving the discrete pressure solution (since it is in the pressure solution that the need for a staggered grid arises). The vertical alignment of the mesh is shown in Figures 2.4 and 2.5. Note that $\overline{w}$ starts at the wall and ends at the top (lid). The other variables (u,v,p,θ,q) begin at $z = \Delta z/2$ and continue at intervals of Δz up to $\Delta z/2$ above the top of the physical domain (i.e. $z = L_z + \Delta z/2$). An exception is that the specified surface values of temperature and moisture content will be referenced to the physical surface (z=0); however, these

Horizontal Directions

Element   1   2   3   4

Node 1   2   3   4   "1"

|————————— 2π —————————|

Vertical Direction

Element   1   2   3

Node 1   2   3   4

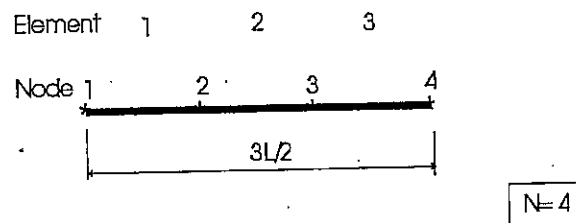|————————— 3L/2 —————————|

N=4
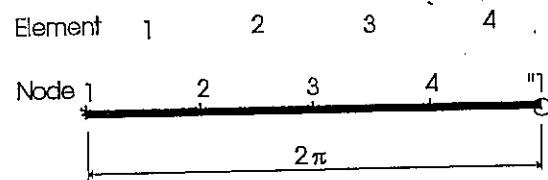
Figure 2.3: Relationship between nodes and internode regions in the horizontal and vertical directions.

are not part of the flow variable arrays. With this approach there remains N_z layers of all the variables. The vertical gradients that must vanish at the top are easily forced by setting the velocity at $\Delta z/2$ above the lid to the value at $\Delta z/2$ below the lid. Again, the main reason for the staggering resides with the pressure solution.

2.3.2 Transformed Variables A pseudospectral approach is one in which operations are done in either physical or spectral space, whichever is more convenient for the given operation (Orszag, 1971). For simulation of the ABL, the horizontal directions are assumed statistically homogeneous and periodic, and can therefore
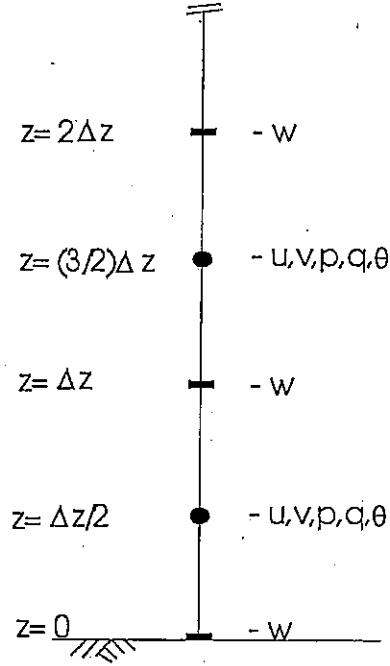
Figure 2.4: Arrangement of primitive variables with respect to the staggered mesh.

be represented well by Fourier polynomials. The vertical direction is inhomogeneous, and certainly not periodic. The major existing LES codes for the ABL (e.g. those of Moeng; Mason; Schumann; and Nieuwstadt) all use finite difference derivatives in the vertical. Finite difference derivatives present several weaknesses when compared with the spectral derivatives, such as significant truncation errors and phase errors (e.g. Malik et al., 1985). Non-periodic boundary conditions for the vertical direction eliminate the Fourier polynomial option, but do not preclude, in general, a spectral approach. In fact, Chebyshev polynomials are naturally suited to the wall-normal direction in shear flows (Orszag, 1971; Fletcher, 1988b). The Chebyshev transform forces enhanced resolution near the boundaries, may be com-
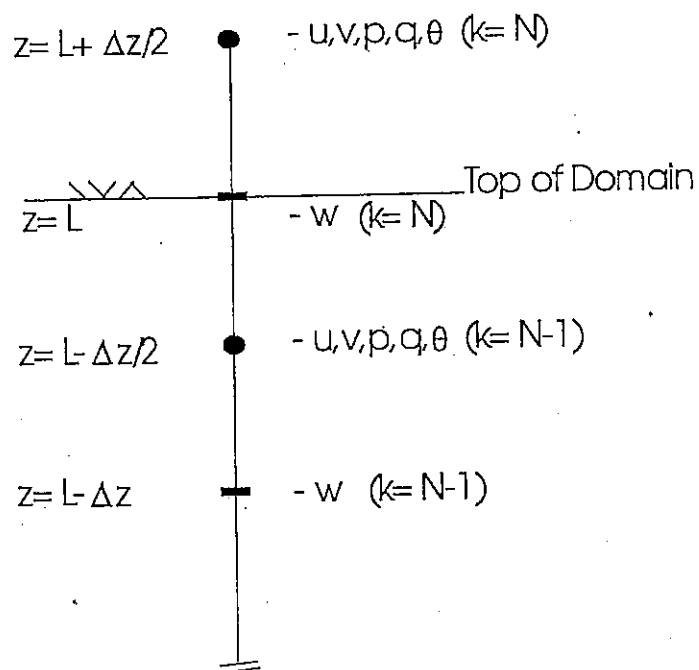
Figure 2.5: Arrangement of primitive variables with respect to the staggered mesh near the top of the domain.

puted with an FFT in $\bigcirc(N_z \ln N_z)$ operations, submits to recursive evaluation of derivative coefficients, and provides infinitely accurate derivatives for fully resolved smooth functions (e.g. Fox and Parker, 1968; Moin and Kim, 1980; Canuto et al., 1988). One drawback to the Chebyshev approach is that the mesh spacing becomes so small near the wall that explicit time advancement requires exceedingly small time steps to maintain numerical stability. A partially implicit treatment yields a full coefficient matrix and is excessively expensive to solve without preconditioning (Malik et al., 1985). Therefore, the version of the LES described here employs second order accurate finite differencing for vertical derivatives, with plans for a future Chebyshev implementation in the vertical with preconditioning.

One exception to the above classification of existing ABL codes, is the direct numerical simulation of the Ekman layer (Reynolds number $\approx$ 100) by Coleman et al. (1994) using Spalart's code with its spectrally accurate Jacobi polynomials in the wall-normal direction. However, there exists no fast-Jacobi transform so their vertical numerics take $O(N^2)$ operations rather than the $O(N \ln N)$ operations of the fast transforms. These expensive calculations limit the number of nodes that can be used in the vertical direction, hence limiting the resolution. Furthermore, their application is of little relevance to the present discussion on the basis of the low Reynolds number.

We can represent a discrete function by either its values in physical space or its corresponding Fourier representation through the expansion in terms of trigonometric functions

$$\bar{u}_i(x, y, z) = \sum_{k_x} \sum_{k_y} \hat{u}_i(k_x, k_y, z) e^{i(k_x x + k_y y)} \tag{2.63}$$

where $\hat{u}_i$ is the complex Fourier amplitude associated with the physical space variable $\bar{u}_i$, k_x and k_y are the wavenumbers in the x and y directions with summations ranging over the integer wavenumbers $-N_x/2 + 1 \leq k_x \leq N_x/2$, and $-N_y/2 + 1 \leq k_y \leq N_y/2$, and $i = \sqrt{-1}$. For this two-dimensional discrete transform it is understood that x and y assume values only at the quadrature points, $x = 2\pi(i-1)/N_x$; $y = 2\pi(j-1)/N_y$, and z remains unconstrained. The transform in (2.63) is invertible (i.e. $\bar{u}_i \Longleftrightarrow \hat{u}_i$) since it is linear and complete in the sense of a Hilbert space (Canuto et al., 1988). Recall that $\bar{u}_i$ is a filtered field,

such that it is fully resolved by the number of modes employed in this finite or truncated transform (2.63). For a general review of discrete Fourier transforms see Press et al. (1992); for a discussion of spectral techniques in fluid mechanics see Canuto et al. (1988); and, for a rigorous presentation of Fourier transforms from a mathematical perspective see Körner (1988).

2.3.3 Spatial Derivatives

The horizontal directions are treated with pseudospectral differentiation and the vertical direction by finite differences.

Horizontal Directions (x,y)   Taking the x and y partial derivatives of (2.63) yields

$$\frac{\partial \bar{u}_i(x,y,z)}{\partial x} = \sum_{k_x}' \sum_{k_y}' [\hat{u}_i(k_x, k_y, z)(ik_x)] e^{i(k_x x + k_y y)} \qquad (2.64)$$

$$\frac{\partial \bar{u}_i(x,y,z)}{\partial y} = \sum_{k_x}' \sum_{k_y}' [\hat{u}_i(k_x, k_y, z)(ik_y)] e^{i(k_x x + k_y y)} \qquad (2.65)$$

where all terms are defined as in (2.63), except we must introduce a modified summation $\sum_{k_{x_i}}'$, were the ($'$) is used to denote a sum over all wavenumbers except the Nyquist wavenumber. For convenience we can represent the terms in the square brackets as $\hat{u}_i'^x$ for (2.64) and $\hat{u}_i'^y$ for (2.65); these primed amplitudes are in fact the Fourier counterparts to the physical space derivatives, i.e. $\frac{\partial \bar{u}_i(x,y,z)}{\partial x} \Longleftrightarrow \hat{u}_i'^x$ and $\frac{\partial \bar{u}_i(x,y,z)}{\partial y} \Longleftrightarrow \hat{u}_i'^y$. The process for computing the derivatives in physical space is by: taking a known set of $\bar{u}_i(x,y,z)$, computing the set $\hat{u}_i(k_x, k_y, z)$ from the equality in (2.63), modifying $\hat{u}_i$ to form $\hat{u}_i'^x$ and $\hat{u}_i'^y$, and finally computing the set of $\frac{\partial \bar{u}_i(x,y,z)}{\partial x}$ and $\frac{\partial \bar{u}_i(x,y,z)}{\partial y}$ from (2.64) and (2.65). This approach is applied to

horizontal planes of nodes (i.e. constant z) taken from the 3D mesh of nodes in the flow domain. Second derivatives are also available from repeated application of the partial derivative operators to (2.64) and (2.65), yielding amplitudes for the second derivatives $\hat{u}_i''^x [= \hat{u}_i(k_x, k_y, z)(-k_x^2)]$ and $\hat{u}_i''^y = [\hat{u}_i(k_x, k_y, z)(-k_y^2)]$.

An often neglected point in descriptions of the pseudospectral differentiation is the need to omit the Nyquist wavenumber from the summations. It is a subtle point that should be explained. The Fourier transform of a real field, such as velocity $\bar{u}_i(x, y, z)$ or any of the other field we may simulate with LES, yields a complex field of amplitudes $\hat{u}_i(k_x, k_y, z)$ that possesses several important characteristics due to the real nature of the original field: (i) the transform is symmetric about the wavenumber origin $\hat{u}_i(-k_x, -k_y, z) = \hat{u}_i^*(k_x, k_y, z)$ (where the * denotes complex conjugate) , (ii) the zero wavenumber amplitude represents the mean value of the function and therefore has only a nonzero real part, and (iii) the amplitude of the highest resolved wavenumber, the so-called Nyquist amplitude, also has only a nonzero real part. It is this third point that is of present interest. In computing the first derivative by the pseudospectral technique we must product the amplitudes by the imaginary number (i), which essentially replaces the real part with the imaginary part (times -1) and replaces the imaginary part with the original real part. Therefore, $\hat{u}_i'^x$ and $\hat{u}_i'^y$ may possess non-zero imaginary parts at the Nyquist wavenumber, from the original real parts, and will, consequently, not satisfy the conditions for the Fourier transform of a real field. If this is overlooked and the Nyquist terms are included in the summation, then the derivative fields in physical

Nyquist amplitude: only real $\xrightarrow{\times i}$ only imaginary $\Rightarrow$ not valid

space will be complex. For this reason the Nyquist amplitude is simply set to zero at both its real and imaginary parts, to effectively omit its inclusion in the double summation of the transform; hence, we only resolve N-1 modes.

In the present code the two-dimensional Fourier transforms are performed with the "fourn" subroutine of Press et al. (1992, p. 518). Consequently, the array structure is as documented in the description by Press et al.

Vertical Direction (z) The derivatives with respect to the vertical direction are by centered finite differencing, with the derivatives referenced to and stored on the half-nodes in between the nodes on which the original variable is stored. That is, vertical derivatives of w are stored on the u, v, p, θ, q nodes and vertical derivatives of u, v, p, θ, q are stored on the w nodes. With loose definition of the vertical index for now, we write the vertical derivatives of $\bar{u}_i$ (as an example) as

$$\frac{\partial \bar{u}_i}{\partial z}(x, y, z) = \frac{\bar{u}_i(x, y, z + \frac{\Delta z}{2}) - \bar{u}_i(x, y, z - \frac{\Delta z}{2})}{\Delta z} \tag{2.66}$$

Figure 2.6 depicts the vertical index (k) for the various primitive variables; note, for example, that $\bar{u}(i, j, k)$ is defined (stored) $\Delta z/2$ above $\bar{w}(i, j, k)$. Hence, we have the following relationships between indices of vertical derivatives and the indices of the original variables

$$\frac{\partial \bar{A}}{\partial z}(i, j, k) = \frac{\bar{A}(i, j, k) - \bar{A}(i, j, k - 1)}{\Delta z}; \quad for \ \bar{A} = \bar{u}, \bar{v}, \bar{p}, \bar{\theta}, \bar{q} \tag{2.67}$$

$$\frac{\partial \bar{A}}{\partial z}(i, j, k) = \frac{\bar{A}(i, j, k + 1) - \bar{A}(i, j, k)}{\Delta z}; \quad for \ \bar{A} = \bar{w} \tag{2.68}$$

A complete vertical referencing of all variables, basic and combinations, and their vertical derivatives is listed below in the algorithm description section.
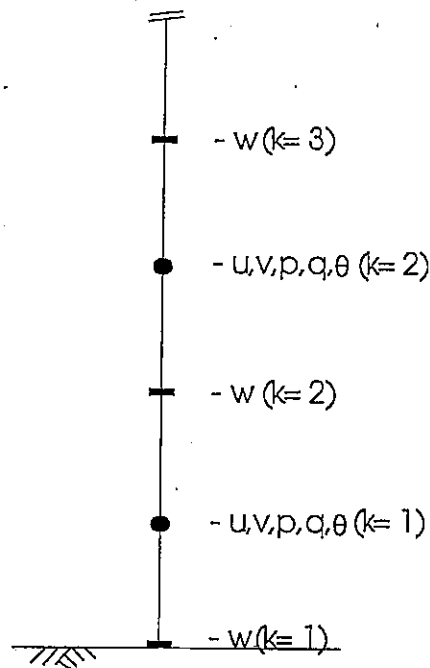
Figure 2.6: Convention for the vertical index with respect to the staggered mesh.

<u>2.3.4 Aliasing</u> As mentioned above, with pseudospectral numerics operations are done in either physical or wave space, whichever is least difficult, more accurate, or less computationally arduous. For example, the horizontal derivatives are computed in the Fourier domain, while local products such as $\bar{u}_j$ times $\delta_j \bar{u}_i$ are computed in physical space, as they would require expensive convolutions in the Fourier domain (see Press et al., 1992). The aliasing arises as we attempt to resolve with say N wavenumbers the product of two variables that are each just resolved with N wavenumbers. For example, we consider the product of two variables A and B and we limit the analysis to one dimension for simplicity of presentation.

Each of the variables can be represented by the discrete Fourier expansion in

terms of the N modes that fully resolve the functions

$$A(x) = \sum_{k=-N/2+1}^{N/2} \widehat{A}(k)e^{ikx} \qquad (2.69)$$

$$B(x) = \sum_{k=-N/2+1}^{N/2} \widehat{B}(k)e^{ikx} \qquad (2.70)$$

for aliasing

and then the product $C(x)$ is exactly

$$C(x) = A(x)B(x) = \sum_{k=-N+1}^{N} \widehat{C}(k)e^{ikx}; \qquad (2.71)$$

where by the convolution theorem we have

$$\widehat{C}(k) = \sum_{m+n=k} \left[\widehat{A}(m)\widehat{B}(n) \right] \quad |m|, |n| \le N/2 \qquad (2.72)$$

Note that because of the convolution in (2.72) the exact Fourier representation of $C(x)$ in (2.71) involves $2N$ modes, rather than the original N. However, with the pseudospectral approach we are not computing $C(x)$ exactly with the convolution and the extended resolution of 2N modes, which would require $O(N^2)$ operations and require twice as many nodes in each direction. Instead, the product $C(x) = A(x)B(x)$ is computed in the physical domain on the N nodes and then an N mode Fourier transform is computed

$$C(x) = A(x)B(x) = \sum_{k=-N/2+1}^{N/2} \widetilde{C}(k)e^{ikx} \qquad (2.73)$$

whereby the information between modes N and $2N$ is aliased or "folded" back to the modes 0 to N. The fully aliased amplitudes $\widetilde{C}(k)$ are related to the correct amplitudes $\widehat{C}(k)$ as

$$\widetilde{C}(k) = \widehat{C}(k) + \underbrace{\sum_{m+n=k\pm N} \left[\widehat{A}(m)\widehat{B}(n) \right]}_{aliasing\ error}; \quad \{-N/2+1 \le k \le N/2\} \qquad (2.74)$$

where the second term on the right hand side is the aliasing error contribution at the kth wavenumber.

In addition to the above general explanation, we need to address whether or not this aliasing in the nonlinear term of the momentum and scalar transport equations poses significant problems. The main points are that: on the numerical theory side, the aliasing errors decay rapidly with increased resolution (larger N); and on the fluid mechanics side, the dissipative nature of the system tends to damp the effects for well resolved systems. Canuto et al. (1988, p. 118) conclude their review of the aliasing error literature in fluid mechanics with the following statement *"Thus, there is reasonable support for the claim that, for a given problem, an aliased calculation will yield just as acceptable an answer as a dealiased one, once sufficient resolution has been achieved."*

One means of completely remove the aliasing errors is by padding or truncation, whereby the Fourier transforms are performed on 3N/2 points and then truncated to N modes (Canuto et al., 1988). With this approach the product of two variables (of N modes each) requires 2N modes for full resolution. Therefore, the transform with 3N/2 modes causes an aliasing of the information between $3N/2 < k \leq 2N$ to the region in wavespace between modes N and 3N/2, which the truncation to N modes completely removes. While this removes all the aliasing errors, it is rather expensive in a computational sense.

The simulations performed for validation of the present code in the following chapter were intentionally of marginal resolution, in order to test critically the nu-

merics and sub grid model (after Andren et al., 1994). It was found in the course of the simulations that aliasing errors were significantly diminishing the accuracy of the results. In consideration of the exponential decay of turbulent energy with increase in wavenumber a partial dealiasing was developed that removes about 90% of the aliasing error but only requires the truncation of 1/8 of the amplitudes (rather than 1/3 truncation with the full dealiasing.) The two-dimensional transforms are performed on (N_x, N_y) modes and are truncated to $(7N_x/8, 7N_y/8)$.

To investigate the performance of the partial de-aliasing we consider a pair of variables A and B, each possessing the analytic spectra $k^{-5/3}$, for $1 \leq |k| \leq 32$. The truncation in the partial de-aliasing is at $|k|=28$. Figure 2.7 compares the fully aliased (no truncation) form and the partially de-aliased form. Note that this figure is focused on the high wavenumber range of the spectrum and thus does not include all the low wavenumber modes. The main point to note from this figure is that the partially de-aliased version (asterixes on circles) nearly coincides with the true spectrum (dashed line) for the resolved range $|k| \leq 28$, whereas the fully aliased spectrum (dotted) is well removed from the true spectrum as k approaches the resolution limit of k=32.

2.3.5 <u>Time Advancement</u> The velocity and scalar fields are integrated in time with the second-order Adams-Bashforth method (Canuto et al., 1988, p.102). This is shown for an arbitrary field, $\overline{A}$, where the conservation equation, i.e. (2.36),(2.37), or (2.38), is written with the local time derivative on the left hand side and all other terms lumped on the right hand side as $\overline{g}$, viz.,

$$\partial_o \overline{A} = \overline{g} \qquad (2.75)$$

With superscripts for time level referencing, the second-order Adams-Bashforth time advancement scheme is

$$A^{t+\Delta t} = A^t + \Delta t \left[\frac{3}{2} \overline{g}^t - \frac{1}{2} \overline{g}^{t-\Delta t} \right] \qquad (2.76)$$

where A^t, $\overline{g}^t$, and $\overline{g}^{t-\Delta t}$ are known. This approach is accurate (Gao and Leslie, 1990) and efficient, with a computational mode that tends to damp favorably (Haltiner and Williams 1980, p. 151).

2.3.6 Pressure Solution   The pressure field in the momentum equation is not a thermodynamic variable, but rather a dynamic variable that serves to maintain a divergence free, or incompressible, velocity field. Consequently, we deduce a pressure field to force the velocity divergence to vanish by taking the divergence of the momentum equation and applying the continuity equation. This leaves us with a Poisson equation for pressure which we can solve numerically, using the spectral transform in the horizontal and finite differences in the vertical.

We begin with the temporally discrete form of the momentum equation

$$\frac{u_i^{t+\Delta t} - u_i^t}{\Delta t} = \frac{3}{2} \overline{RHS_i}^t - \frac{1}{2} \overline{RHS_i}^{t-\Delta t} \qquad (2.77)$$

where RHS_i is written for the discrete (numerical) form of $-\overline{\bar{u}_j(\partial_j \bar{u}_i - \partial_i \bar{u}_j)} - \partial_i \overline{p} + F_p \delta_{i1} - \partial_j \tau_{ij} + \beta \delta_{i3}$. It is instructive to break the present time step's pressure gradient out of RHS_i^t, such that $RHS_i^t = -\partial_i \overline{p}^t + \Gamma_i^t$ and (2.77) becomes

$$\left(\frac{2}{3\Delta t}\right) u_i^{t+\Delta t} + \partial_i \bar{p}^t = \left(\frac{2}{3\Delta t}\right) u_i^t + \Gamma_i^t - \frac{1}{3}\overline{RHS_i}^{t-\Delta t} \qquad (2.78)$$

with unknown quantities collected on the left. Note that (2.78) is the exact form

of the momentum equation used to advance the velocity field. The objective in the

pressure solution is to define a pressure field such that $\partial_i \bar{p}^t$ in coordination with

the known values of u_i^t, Γ_i^t, and $\overline{RHS_i}^{t-\Delta t}$, will yield a divergence free $u_i^{t+\Delta t}$. We

seek the pressure field by first taking the divergence of (2.78) to obtain

$$\left(\frac{2}{3\Delta t}\right) \partial_i u_i^{t+\Delta t} + \partial_i \partial_i \bar{p}^t = \partial_i \left[\left(\frac{2}{3\Delta t}\right) u_i^t + \Gamma_i^t - \frac{1}{3}\overline{RHS_i}^{t-\Delta t} \right] \qquad (2.79)$$

in which $\partial_i u_i^{t+\Delta t}$ should be set identically to zero in order to solve for the appropri-

ate pressure field; however, we include the potentially finite $\partial_i u_i^t$ from the previous

time step (say from poor initial conditions or numerical errors). With $\partial_i u_i^{t+\Delta t}$ re-

moved and Λ_i written for $\left[\left(\frac{2}{3\Delta t}\right) u_i^t + \Gamma_i^t - \frac{1}{3}\overline{RHS_i}^{t-\Delta t} \right]$ the Poisson equation for

pressure is obtained

$$\partial_i \partial_i \bar{p}^t = \partial_i \Lambda_i \qquad (2.80)$$

where the known Λ_i is used to solve for $\bar{p}^t$, subject to appropriate boundary con-

ditions.

Toward a solution the Poisson equation is written with x and y directions

represented spectrally and the z direction numerics left in general operator form

$$\sum_{k_x}\sum_{k_y}[\widehat{p}(k_x, k_y, z)(-k_x^2) + \widehat{p}(k_x, k_y, z)(-k_y^2) + \partial_3 \widehat{p}(k_x, k_y, z)]e^{i(k_x x + k_y y)} \qquad (2.81)$$

$$= \sum_{k_x}\sum_{k_y}[\widehat{\Lambda}_1(k_x, k_y, z)(ik_x) + \widehat{\Lambda}_2(k_x, k_y, z)(ik_y) + \partial_3 \widehat{\Lambda}_3(k_x, k_y, z)]e^{i(k_x x + k_y y)} .$$

which implies for the orthogonal functions that for each (k_x, k_y, z) the following must be satisfied

$$\widehat{p}(-k_x^2) + \widehat{p}(-k_y^2) + \partial_3 \widehat{p} = \widehat{\Lambda}_1(ik_x) + \widehat{\Lambda}_2(ik_y) + \partial_3 \widehat{\Lambda}_3 \qquad (2.82)$$

where the explicit referencing of the amplitudes to (k_x, k_y, z) has been dropped and remains implied. Through the horizontal spectral transform, (2.80) has been reduced from a partial differential equation for $\bar{p}$ in x, y, and z to an ordinary differential equation for $\widehat{p}$ in z. In its general form, (2.80) requires boundary conditions to be specified on all faces of the domain; however, the spectral transform with the implied periodicity in the horizontal limits the need for explicit boundary conditions to the vertical directions (c.f. (2.82)). Vertical boundary conditions are available from consideration of the vertical momentum balance across the upper and lower boundaries. Ignoring local buoyant forcing, (2.36) written across the lower and upper boundaries for $i = 3$, and Fourier transformed, is

$$\partial_3 \widehat{p} = -\partial_j \widehat{\tau}_{zj} \; ; \quad z = 0, \; and \; L_z \qquad (2.83)$$

Hence we have an analytic boundary value problem. The Poisson equation (2.82) must be satisfied at all levels (heights) inside the flow domain, and (2.83) must be satisfied across the bottom and top boundaries (i.e. across the planes $z = 0$ and $z = L_z$). Hence, (2.82) is written at each of the u,v,p nodes in the range $1 \leq m \leq N_z - 1$, and (2.83) is written at the w nodes referenced as $m = 1 \; and \; m = N_z$; see Figures 2.5 and 2.6 for the node referencing.

The first vertical derivative of $\widehat{\Lambda}_3$ in (2.82) is represented by (2.68), with $\widehat{\Lambda}_3$

$$(2.67) \qquad \frac{\partial \bar{A}}{\partial z}(i,j,k) = \frac{\bar{A}(i,j,k) - \bar{A}(i,j,k-1)}{\Delta z}$$

referenced to the w nodes and its vertical derivative referenced to the u,v,p nodes. The first vertical derivative of $\widehat{p}$ in the boundary condition (2.83) is represented by (2.67), with $\widehat{p}$ referenced to the u,v,p nodes and its vertical derivative referenced to the w nodes. The second vertical derivative is by the following second order accurate centered differencing scheme

$$\partial_3 \widehat{p}(k_x, k_y, m) = \frac{\widehat{p}(k_x, k_y, m+1) - 2\widehat{p}(k_x, k_y, m) + \widehat{p}(k_x, k_y, m-1)}{\Delta z^2} \qquad (2.84)$$

with both $\widehat{p}$ and its second derivative referenced to the u,v,p nodes (i.e. all terms of (2.82) are referenced to u,v,p nodes and the boundary conditions (2.83) are on the w nodes). In their discrete form, (2.82) has a vertical support of $z - \Delta z \ to \ z + \Delta z$ and (2.83) has a vertical support of $z - \Delta z/2 \ to \ z + \Delta z/2$. Therefore, an additional pressure node is introduced at $z = -\Delta z/2$, referenced as $m = 0$ in Figure 2.8. Also shown in this Figure are the equation stencils (I for the interior Poisson equation (2.82) and BC for the boundary condition (2.83)), note that I includes $\widehat{p}(m-1), p(m),$ and $\widehat{p}(m+1)$ for $1 \le m \le N_z - 1$, the lower BC includes $\widehat{p}(0)$ and $\widehat{p}(1)$, and the upper BC includes $p(N_z - 1)$ and $p(N_z)$. With $\widehat{\Lambda}_i$ known this represents a tridiagonal system of $N_z + 1$ equations for the vertical series $\widehat{p}$ (for each wavenumber pair (k_x, k_y)), which we can write as

$$\widehat{p}_{m+1}\left(\frac{1}{\Delta z^2}\right) + \widehat{p}_m\left(-\frac{2}{\Delta z^2} - k_x^2 - k_y^2\right) + \widehat{p}_{m-1}\left(\frac{1}{\Delta z^2}\right) = r_m; \qquad (2.85)$$

$$1 \le m \le N_z - 1$$

$$\widehat{p}_1\left(\frac{1}{\Delta z}\right) - \widehat{p}_0\left(\frac{1}{\Delta z}\right) = -\partial_j \tau_{zj(z=0)} \quad (2.86) \qquad (z = 0)$$

$$\widehat{p}_{N_z}\left(\frac{1}{\Delta z}\right) - \widehat{p}_{N_z-1}\left(\frac{1}{\Delta z}\right) = -\partial_j \tau_{zj(z=L_z)} (2.87) \qquad (z = L_z)$$

where r_m is written for the known quantity $\widehat{\Lambda}_1(ik_x) + \widehat{\Lambda}_2(ik_y) + \frac{\widehat{\Lambda}_3(m+1)-\widehat{\Lambda}_3(m)}{\Delta z}$ centered on node m, and $\widehat{p}_m$ is written for the pressure amplitude $\widehat{p}(k_x, k_y, m)$. This system of equations (coupled in z) can be solved uniquely for the cases where k_x and k_y are not both equal to zero. However, the system does not yield a unique solution for the zero wavenumber case, which represents the horizontal mean pressure at each height, where by "pressure" we refer to the combination of variables described in (2.18). For this zero wavenumber case we use a simple vertical integration of the horizontally averaged vertical pressure gradient, which is available from the horizontally averaged vertical momentum equation,

$$\widehat{p}(0,0,m) = \widehat{p}(0,0,m-1) + \Delta z \left[\widehat{\Lambda}_3(0,0,m) \right] \qquad (2.88)$$

where $\widehat{\Lambda}_3(0,0,m)$ is referenced on the w nodes centered between $\widehat{p}(0,0,m)$ and $\widehat{p}(0,0,m-1)$, and the average pressure at the bottom boundary is set to an arbitrary value $(\widehat{p}(0,0,0) = 0)$ to start the integration. This boundary value is irrelevant since only gradients of pressure are used in the momentum equations. With the pressure amplitudes $\widehat{p}(k_x, k_y, m)$ computed for all wavenumbers the pressure values in physical space are computed from the inverse Fourier transform.

A subtle point in the Poisson solution is that there must be absolute consistency in the numerics in order for the derived pressure field to remove any pre-existing velocity divergence. For example we consider the case where the velocity field possesses a finite divergence

$$\partial_i \overline{u}_i = \delta \qquad (2.89)$$

that must be removed by the pressure gradients. For illustration we represent the

velocity as the sum of solenoidal and divergent fields

$$\overline{u}_i = \overline{u}_i^s + \overline{u}_i^d \qquad (2.90)$$

where, by definition,

$$\partial_i \overline{u}_i^s = 0 \qquad (2.91)$$

$$\partial_i \overline{u}_i^d = \delta \qquad (2.92)$$

The Poisson solution is charged with deducing a pressure field with gradients that will remove $\overline{u}_i^d$. That is, the pressure gradient in the x_i direction should affect a velocity acceleration that when integrated over the time step yields in itself a velocity increment of $-\overline{u}_i^d$, that when added to $\overline{u}_i$ will total to the solenoidal field $\overline{u}_i^s$, i.e.

$$(-\partial_i p) \Longrightarrow -\overline{u}_i^d \qquad (2.93)$$

Recall in the Poisson solution that the Laplacian of the pressure is affected by the divergence of the velocity field, as we see by applying the ∂_i operator to (2.93)

$$\underbrace{\partial_i}_{I} \overline{u}_i^d \Longrightarrow \underbrace{\partial_i}_{II} \left[\underbrace{\partial_i}_{III} p \right] \qquad (2.94)$$

Where the need for consistency arises is that the actual discrete operators referenced above as I and II must be identical, and the repeated operation of the first derivative operator (II on III) must be identical to the second derivative operator used in the Poisson solver in order for the deduced pressure field to remove the velocity divergence. This consistency is achieved in the horizontal directions without ambiguity by the Fourier numerics. However, this consistency is achieved with the

vertical derivative operators in the present algorithm by design, using a staggered grid and centered differencing.

2.4 Solution Algorithm

Variable names from the LES code and their descriptions are listed in Appendix A. An outline of the subroutine names, the variables passed to them, the variables returned, and the routines that are called within each subroutine is attached as Appendix B. The FORTRAN source code is attached as Appendix C. Note that general simulation parameters, such as the number of nodes, are defined in the include file "dimen.h", which is listed with the source code in Appendix C. The variables are referenced to the staggered grid as below

Variable	U,V,P Nodes	W Nodes
u, v, p, θ, q	x	
w		o
$\partial_x u, \partial_y u, \partial_x v, \partial_y v$	x	
$\partial_z u, \partial_z v$		o
$\partial_x w, \partial_y w$		o
$\partial_z w$	x	
$\partial_x p, \partial_y p$	x	
$\partial_z p$		o
$\partial_x \theta, \partial_y \theta, \partial_x q, \partial_y q$	x	
$\partial_z \theta, \partial_z q$		o
$\tau_{xx}, \tau_{xy}, \tau_{yy}, \tau_{zz}$	x	
τ_{xz}, τ_{yz}		o
$\pi_x^\theta, \pi_y^\theta, \pi_x^q, \pi_y^q$	x	
π_z^θ, π_z^q		o
$\partial_j \tau_{xj}, \partial_j \tau_{yj}$	x	
$\partial_j \tau_{zj}$		o
C_x, C_y	x	
C_z		o
$< uw >, < vw >$		o
ν_T	x	

Initial conditions for the velocity and scalar fields are either generated by a

call to a subroutine or the full matrices are read from the files "vel.out", "t.out" and "q.out". Generally, the fields are generated for the first run and then subsequent runs receive initial fields from these files using the final fields written at the termination of the previous run.

During each time step the following flow is followed

- Velocity and scalar fields are Fourier filtered for the partial dealiasing

- The right hand side matrices of the momentum and scalar conservation equations from the previous time step are saved for use in the Adams-Bashforth time advancement.

- Velocity and scalar gradients are calculated

- The wall stress is calculated

- The z derivatives of u and v are calculated for the first level of nodes above the wall

- The divergence of the velocity field is computed

- The (rotational) convective terms are calculated

- The eddy viscosity is calculated

- The sub-grid stresses and their divergences are computed

- The pressure field is deduced

- The pressure gradients are calculated

- The right hand side matrices are compiled from the individual terms

- The conservation equations are integrated in time .

- Fields are sampled for the calculation of simulation statistics

At the end of each averaging period (as defined by the variable P_COUNT in file dimen.hH) the summary statistics are averaged and written to output files.

At the end of the full time integration (as defined by the variable NUM-STEPS in file DIMEN.H) the instantaneous velocity and scalar fields are written to "vel.out", "t.out" and "q.out".
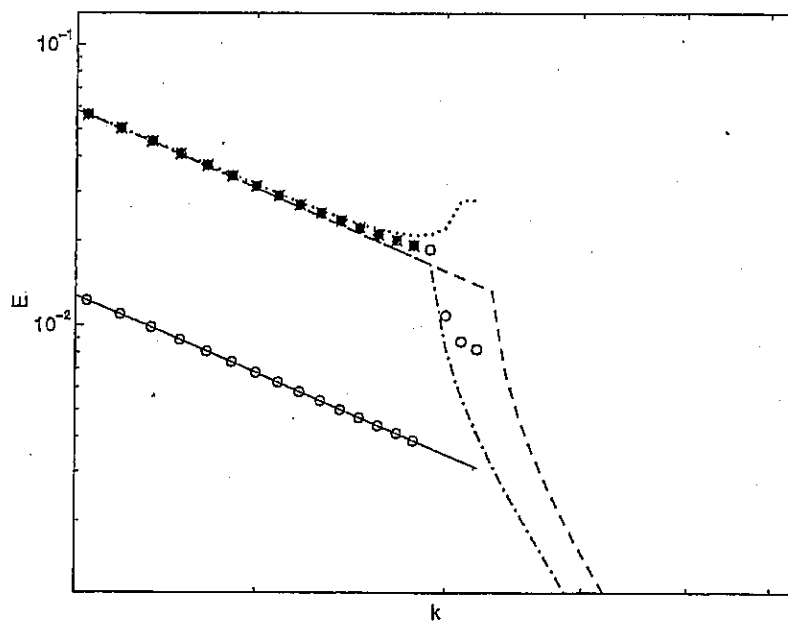
Figure 2.7: Comparison of the fully aliased and partially dealiased cases. The solid line represents a $k^{-5/3}$ spectrum (Functions A and B); the circles on the solid line show the 7/8 truncated spectrum of A and B; The dashed line is the full transform of AB, fully resolved and filling 2N wavenumbers; the dotted line is the aliased version of this AB function; The dot-dashed line is the square of the truncated spectrum; the circles near the top show the partially aliased spectrum; and, the asterixes in the circles show the truncated (filtered) version of the partially dealiased case.
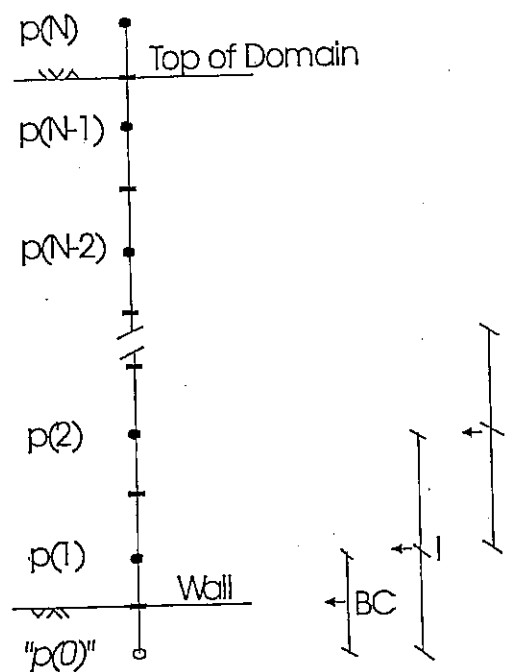
Figure 2.8: Arrangement of pressure nodes for Poisson solution. BC denotes the stencil for the boundary condition equation, and I denotes the stencil for the interior Poisson equations.

CHAPTER 3

Validation of the Neutrally Stratified Case

3.1 Introduction

The initial applications of the present code are for the neutrally stratified boundary layer case, where the code will be employed to identify the effects of patches of variable surface roughness on the spatial averages of surface stress or momentum flux across the land-atmosphere interface. In this chapter we examine and test the performance of the LES to simulate the resolved field and effectively model the sub-grid effects for the neutral case. Toward this end we attempt to simulate the neutrally stratified atmospheric boundary layer (ABL) in a large flow domain with rather coarse resolution. The coarse resolution is adopted to (i) resolve minimally the large scale field so as to test critically the numerics, (ii) to force a significant amount of the energy into the sub-grid field in order to test the sub-grid scale (SGS) model's performance, and (iii) to provide similar resolution as a recent comparison of LES codes for the simulation of the neutral ABL by Andren et al. (1994).

Our intended use of the LES code in its present form is to study the horizontal aggregation of surface exchange over spatially variable surfaces. Consequently, we have ignored for now the effects due to the Earth's rotation, since these effects are not appreciable in the surface layer of the ABL (e.g. Kaimal and Finnigan, 1994). And while we do not believe that this will adversely affect the results, it

does to a small extent blur the comparison of our results to those of Andren et al. (1994), who simulated the neutrally stratified Ekman layer including the turning of the velocity field with height. To sharpen the comparison we will also consider the results of Moin et al. (1978), who studied neutrally stratified channel flow (without turning) with an LES code similar in many ways to the one used here.

3.1.1 Objectives We seek to validate the performance of the LES to simulate the ABL with respect to mean flow variables, variances, stress, and power spectra for the neutrally stratified case. It is impossible to validate LES results in a complete sense. However, we can establish that certain important statistics behave as we would expect for a turbulent boundary layer. Perhaps equally important, we seek to confirm that the present LES produces results similar to select previously published LES codes. This last point is simplified by the recent comparison publication of Andren et al. (1994) and the availability of the comprehensive report of Moin et al. (1978).

The specific objectives are to compare the LES results to published results for the following basic characteristics/statistics: mean velocity profiles, profiles of resolved field velocity standard deviations, resolved and sub-grid vertical momentum flux profiles, and velocity power spectra.

3.2 Flow Description

The simulated flow is a neutrally stratified boundary layer, driven by a mean streamwise pressure gradient that is constant in space and time and capped by

a stress-free and rigid lid. The production of turbulence is by shearing in this case, with "production eddies" being both smaller than those in the convective case and more concentrated near the wall (e.g. see Tennekes and Lumley, 1972). Therefore, a greater amount of the information resides in the sub-grid field and must be handled with the sub-grid model, thus making this a difficult test for an LES code.

The surface is defined by a constant surface roughness of 0.1 m and a friction velocity of 0.45 m/s (as in Andren et al., 1994).

3.3   Simulation Characteristics

3.3.1   Domain/Extent   The simulation domain extends 1500 m in the vertical and 4000 m in each of the horizontal directions. For this problem, Andren et al. (1994) simulated 1500 m in the vertical, 4000 m in the streamwise, and only 2000 m in the spanwise direction. However, the present LES code is constrained to equal horizontal domain dimensions of $2\pi z_s$, such that the dimensionless length in each of the horizontal directions is 2π.

3.3.2   Resolution   Andren et al. (1994) employed 40 nodes in each direction. Our LES, because of the choice of fast Fourier transform routine, is presently constrained to integer powers of 2 for the number of nodes in each the x and y directions. The simulation described in this chapter employed 32x32x40 nodes with a dimensional resolution of 125 m x 125 m x 38 m in the x, y, and z directions, respectively. Recall the one exception, that the first horizontal plane of nodes is

located a height of $\Delta z/2$ above the wall.

3.3.3 Initial Conditions

The initial conditions for the simulation consist of a modified logarithmic velocity profile with a prescribed turbulent kinetic energy (TKE) profile superimposed on the mean profile. The mean profile is logarithmic in the surface layer, but is forced to reach a zero vertical gradient at $z = (1000 \, m)/z_s$ and to remain constant for $z > (1000 \, m)/z_s$. This was achieved by reducing the log-profile velocity gradient by a multiple of z, such that $\partial_3 < \overline{u}_1 > \rightarrow 1/kz$ as $z \rightarrow 0$ and $\partial_3 < \overline{u}_1 > \rightarrow 0$ as $z \rightarrow (1000 \, m)/z_s$, above which height the gradient is kept at zero.

$$\partial_3 < \overline{u}_1 > = \frac{1}{kz} - \alpha z; \quad z \leq 1000 \, m/z_s \tag{3.1}$$

$$\partial_3 < \overline{u}_1 > = 0; \quad z > 1000 \, m/z_s$$

and selecting $\alpha \left[= \frac{1}{k(1000 \, m \, /z_s)^2} \right]$ to force $\partial_3 < \overline{u}_1 > \rightarrow 0$ at $z = (1000 \, m)/z_s$. Integrating this gradient yields a mean velocity profile of

$$< \overline{u}_1 > = \frac{1}{k} \ln(z/z_o) - \frac{\alpha}{2} z^2; \quad z \leq 1000 \, m/z_s \tag{3.2}$$

$$< \overline{u}_1 > = \frac{1}{k} \ln([(1000 \, m)/z_s]/z_o) - \frac{\alpha}{2} [(1000 \, m)/z_s]^2; \quad z > 1000 \, m/z_s$$

The transverse and vertical velocities are forced to

$$< \overline{u}_2 > = 0; \quad all \, z \tag{3.3}$$

$$< \overline{u}_3 > = 0; \quad all \, z$$

The vertical profile of resolved TKE is taken from Andren et al. (1994, Table A.1). The instantaneous velocities $\overline{u}_i(x, y, z)$ are obtained by distributing the

TKE randomly between the components and randomly in space onto the mean profiles. The portion of the code dealing with the scalar fields was turned off for this simulation.

3.3.4 Scales

The scaling length z_s was chosen as 637 m such that the dimensionless horizontal domain lengths are 2π. The friction velocity u_* implied by the roughness length and prescribed velocity profile in the surface layer is 0.45 m/s. A summary of the scaling variables is given below.

Scale	Value
length, z_s	637 m
velocity, u_*	0.45 m/s
time, $t[= z_s/u_*]$	1415 s

The output of the simulation is in dimensionless form, and is scaled to dimensional form as needed through producting by u_* for velocities, t for times, u_*^2 for velocity variances, and $u_* z_s$ for the eddy viscosity, for example.

3.3.5 Boundary Conditions

The horizontal directions have implied periodic boundary conditions from the pseudospectral numerics, the top boundary is a rigid and stress-free lid as described in Chapter 2, and the bottom boundary is handled with the boundary conditions and wall functions described in Chapter 2 with a homogeneous surface roughness of 0.1 m.

3.3.6 Sub Grid Model The sub-grid model is the Smagorinsky eddy viscosity model, with one exception from the description of Chapter 2: for the poor resolution of 40 nodes in the vertical over 1500 m, the asymptotic wall model produces erroneously low sub-grid stress at the first node above the wall and, consequently, the resolved turbulence grows excessively large. Therefore, for these validation cases the length scale in the eddy viscosity model is taken as a constant equal to the vertical mesh spacing. The Smagorinsky constant, C_s, was arbitrarily set to a value of 0.2 (a value typically reported in the literature). At present no systematic calibration of the sub-grid model has been performed.

3.3.7 Time Integration The time step is limited by stability concerns for the explicit time advancement. The dimensionless time step must be well less than $\Delta x/\bar{u}_1 [\approx \frac{2\pi/N_x}{\bar{u}_{1\,max}}]$. It was found that a stable integration could be achieved with $\Delta t = 0.001$ for this case where $N_x = 32$. The dimensional time step (scaled by t) is $\Delta^d t = 1.42$ s.

The codes used in Andren et al. (1994) are able to employ a longer time step by imposing a Galilean transformation on the coordinate system. This essentially moves the mesh along with the flow to reduce the relative velocity between the fluid and the mesh. We have chosen not to employ such a technique, as this code has been developed for use with spatially variable surface conditions. If the mesh were to move over the fixed surface properties there would be a loss of spatial resolution of the sharp transitions in surface properties, as the mesh would move a fraction of a node spacing over each time step and then after finally translating

one full node the edge would be instantaneously shifted to the next node.

The velocity fields are integrated in time for 25 dimensionless time units (25,000 steps), at which time the TKE field had well reached an apparent stationarity. This period of 25 dimensionless time units is referred to as the spin-up time, during which the memory of the initial conditions is lost and the flow develops the correlations between the velocity components and the proper scaling of statistics from the wall to the lid as we expect for a shear-driven turbulent boundary layer. Immediately following the spin-up period the flow was integrated for another 10 dimensionless time units for sampling and averaging of the statistics for the comparison/validation. The spin-up period corresponds to about 10 hours and the averaging period to 4 hours. Andren et al. (1994) ran their simulations for a spin-up period of 20 hours and a subsequent averaging period of 8 hours.

3.4   Results and Discussion

The statistics in this section (save the spectrum) all represent vertical profiles, where the values at each height are derived from averages over the full horizontal extent of the domain and over the ten dimensionless time units of the integration. The horizontal velocity components are shown in Figures 3.1 and 3.2. The vertical velocity component has a horizontal mean that is identically zero at all heights and times, due to removal of the hydrostatic equation from the vertical momentum equation.

The longitudinal velocity in Figure 3.1 is similar to the prescribed initial velocity profile in the lower third of the domain, but represents higher velocities than
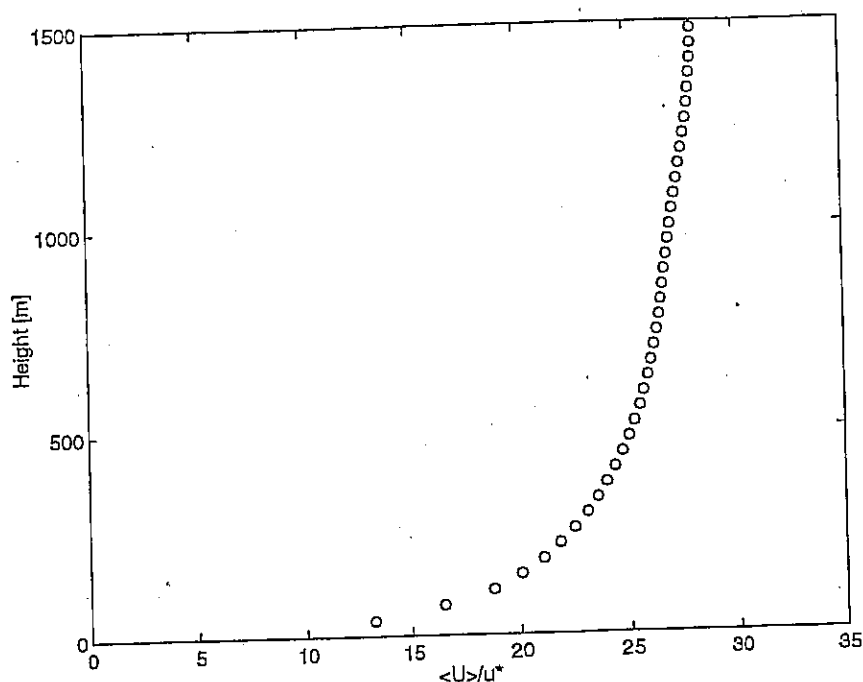
Figure 3.1: Mean longitudinal velocity component.

prescribed in the outer region. The outer region velocities grew in time during the early period of the spin-up, but reached a steady state before the spin-up was complete. This is an expected result, for without straining (gradients) due to buoyant motion or turning from Coriolis, the mean pressure forcing causes the outer region velocity to grow until velocity gradients are strong enough to support sufficient drag through the eddy viscosity as needed to balance the forcing. Without a vertical velocity gradient the x-momentum introduced through the pressure forcing would not be transported toward the wall. Hence, through the spin-up process the arbitrarily defined initial conditions have been replaced with a mean field that is more appropriate for the flow conditions being simulated. Note also that the applied TKE profile (after Andren et al., 1994) vanishes for the upper half of the
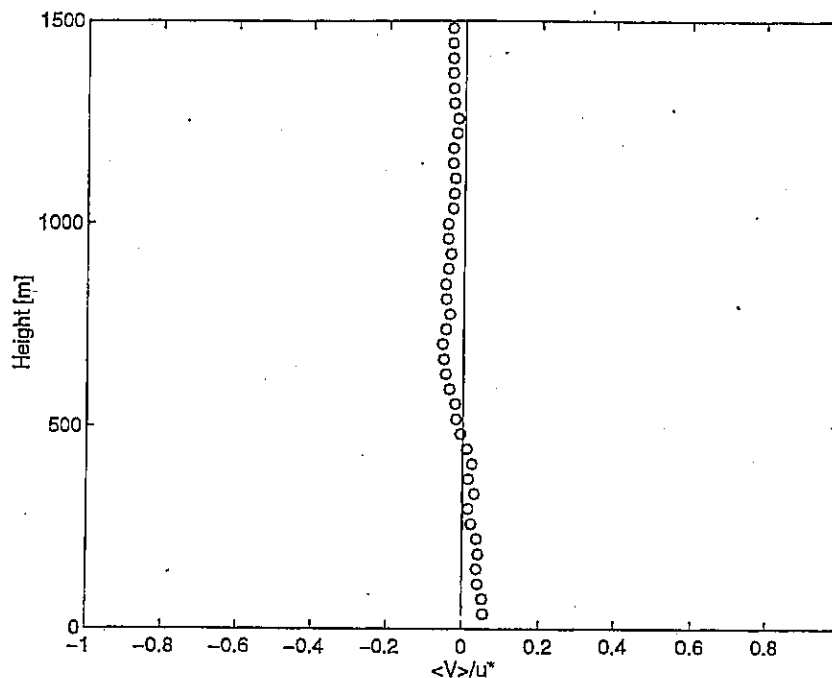
Figure 3.2: Mean transverse velocity component.

simulation domain; consequently, there are no initial turbulent gradients to create a non-zero eddy viscosity in this region during the early periods of the integration. The lateral velocity in Figure 3.2 stays essentially as it began, that is a zero horizontal mean value at all heights.

The vertical profile of the standard deviation of the resolved longitudinal velocity component (normalized by the friction velocity u_*) is shown in Figure 3.3 along with published values for comparison. The circles are from the present LES, the region between the solid lines delineates the range of results from the four codes used to simulate the Ekman layer in Andren et al. (1994, hereafter A94), and the crosses mark the profile for the neutrally stratified channel flow simulation of Moin et al. (1978, hereafter M78). Before comparing results it is necessary to consider

several specific points about the individual studies compared here. The results of M78 have been scaled vertically to equate the vertical extent of the present simulation with their half-channel width. In the near wall region M78 employed fine vertical mesh resolution, thus resolving a large fraction of the turbulence even in the wall region. The cross marks on this Figure (and those following) are a subset of the vertical nodes in M78, shown here simply to establish the general vertical structure of their results. In comparing the present results to the ABL simulations of A94 it is important to note that A94 included the Coriolis term which turns the direction of the mean flow from the x toward the y direction for larger values of z. This may be a partial explanation for why our simulation has more energy in the longitudinal component of the velocity at large heights. With this said, we now compare the results, beginning at the wall and moving upward. Our simulation and those of A94 have coarse resolution such that much of the near wall energy is in the sub-grid scales. Therefore, these simulations have resolved variances that grow with z up to a point where z is large enough (say 100 or 200 m) that most of the turbulence is resolved. M78, with their finer wall resolution captures more variance in the resolved scales near the wall. All of the simulations have variances decaying with height, with greatest decay in the Ekman simulations of A94. At mid-heights there is about a 25% greater magnitude of the fluctuations in the $\overline{u}_1$ field for our simulations than for M78, which may be due to either (i) the lack of Coriolis, a capping inversion, or a no-slip opposing wall as in the channel case, such that we see strong vertical gradients of the mean longitudinal velocity in the outer region

(described above for the mean profile) which act to produce an excess of energy in the local turbulence fields; or (ii) the Smagorinsky constant set equal to 0.2 may not be optimal for our LES. This last point will be addressed with further tests and a planned calibration study for the pressure forcing and the Smagorinsky constant. The top two nodes in the present simulation have erroneously high energy content. We believe this is due to the particular implementation of the boundary conditions inhibiting the damping of numerical errors. This is a problem that will be addressed in future modifications of the code, but should not affect the present efforts to simulate the interaction of the ABL and the land surface.
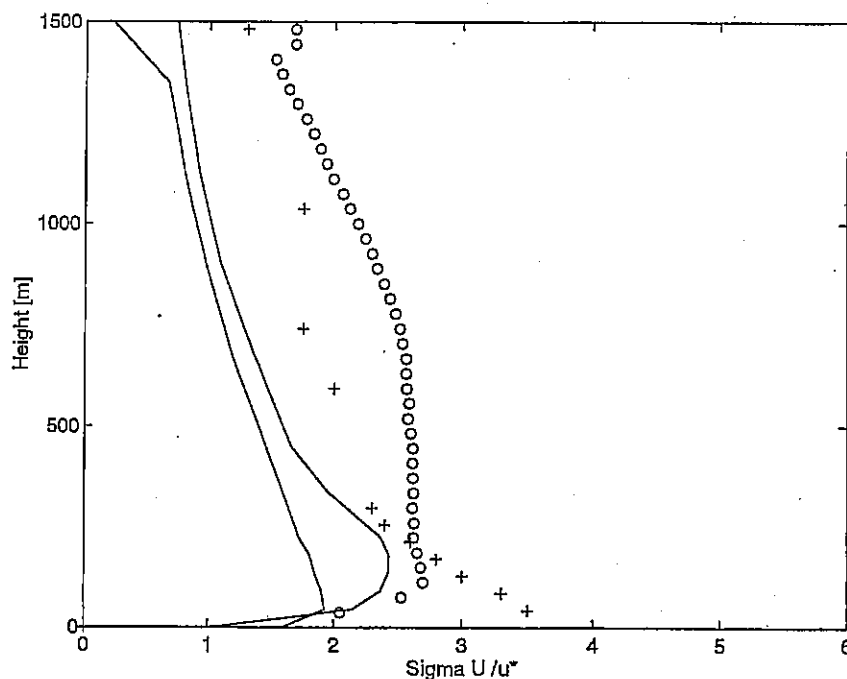
Figure 3.3: Standard deviation of resolved longitudinal velocity component ('o'), the range of results from Andren et al. (1994) between the solid lines, and results of Moin et al. (1978) follow the '+' marks.

In its present form our LES does not provide diagnostic information regarding the sub-grid variances. Therefore, no attempt has been made to compare total variances in this section. Obtaining sub-grid variances is made problematic by the removal of the trace of the sub-grid stress tensor (as described in Chapter 2). However, it is possible to employ empirical diagnostic formulae to deduce estimates of the sub-grid variances from the quantities that are provided by the LES.

In Figure 3.4 we show the vertical profile of the standard deviation of the resolved transverse velocity component (normalized by the friction velocity u_*). Again, the circles are our LES, the A94 results fall in the region between the solid lines, and the crosses mark the results of M78. All of the results compare fairly well for the lower half of the domain, but then our results fail to decay as fast as the others toward the top. In general, the comparison is acceptable. Most likely the planned SGS model calibration study mentioned above will serve to correct this discrepancy as well.

Figure 3.5 shows the vertical profile of the standard deviation of the resolved vertical velocity component (normalized by the friction velocity u_*). The symbols are as described for σ_u and σ_v. Our results very nearly match those of the half-channel results from M78, with the exception that our upper boundary condition forces $\overline{w}$ to 0 at the top. In general these results seem acceptable.

The vertical structure of the eddy viscosity of the sub-grid scale motion is shown in Figure 3.6, with our results marked by circles and the results of A94 bounded by the solid lines. For comparison to A94, which reports an eddy dif-
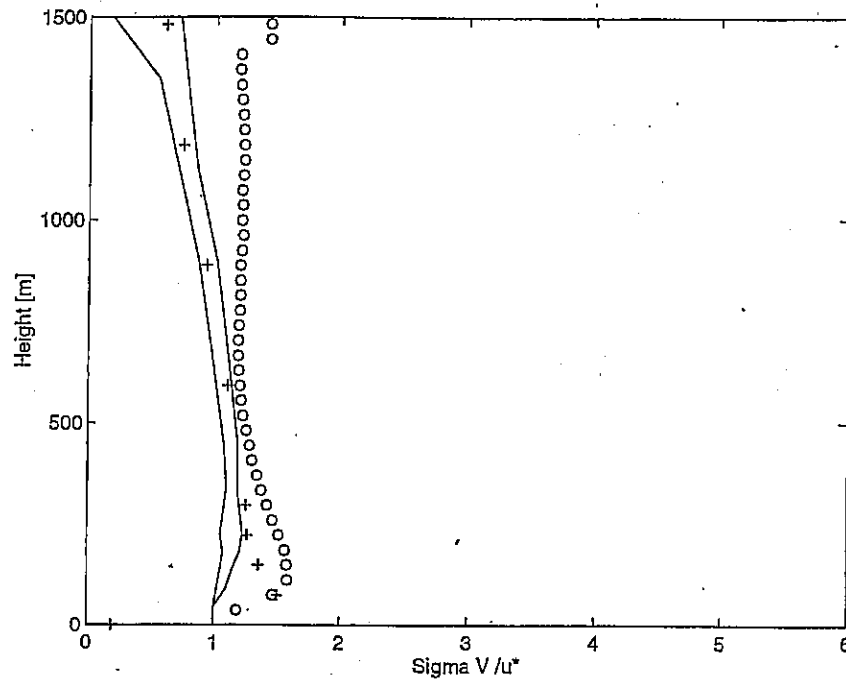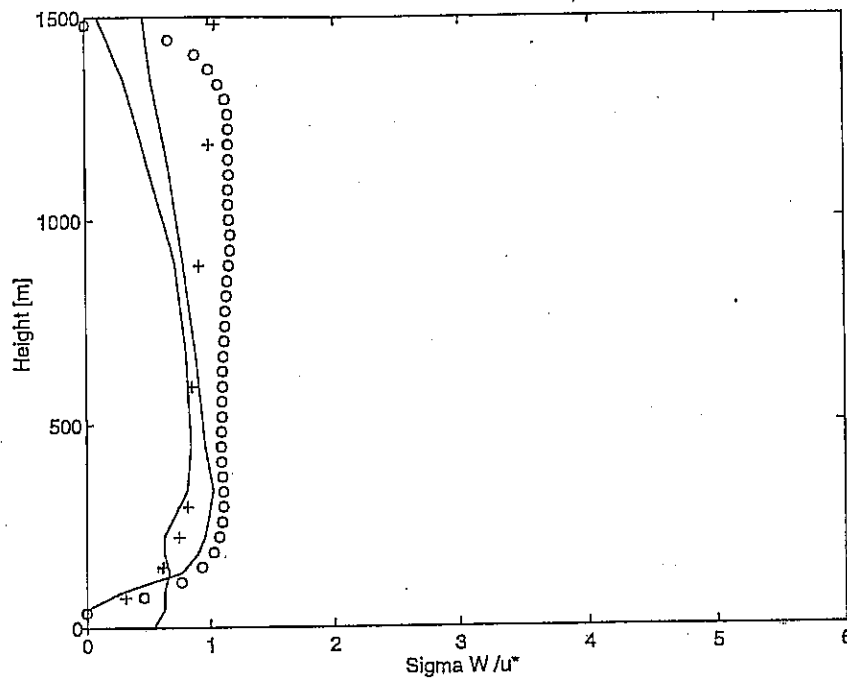
Figure 3.4: Standard deviation of resolved transverse velocity component ('o'), the range of results from Andren et al. (1994) between the solid lines, and results of Moin et al. (1978) follow the '+' marks.

fusivity for momentum in dimensional terms, we have scaled our dimensionless results by $z_s u_*$. Our profile of eddy viscosity falls generally within the bounds of the A94 results. One potential difference in the structure is that both the upper and lower bounds of A94 are decreasing with height (as are their variances), whereas our ν_t results are fairly constant with height above z=400 m (as are our variances). In considering this figure in combination with those for the standard deviations of the velocity components, it appears that our selected values for the Smagorinsky constant and/or the sub-grid length scale may be too low. That is, we have larger magnitudes for our velocity fluctuations, yet equivalent eddy viscosity

Figure 3.5: Standard deviation of resolved vertical velocity component ('o'), the range of results from Andren et al. (1994) between the solid lines, and results of Moin et al. (1978) follow the '+' marks.

magnitudes to A94. The larger velocity fluctuations should logically translate into larger strain rates, which would in turn yield higher values for ν_t, *ceteris paribus.* That we do not see the higher eddy viscosities implies that the sub-grid model requires calibration (i.e. improved values for l and C_s).

Perhaps the most important test for the immediate applications of this LES code is its ability to accurately simulate and model the downward flux of momentum through the ABL toward the rough land surface. These results are shown in Figure 3.7, with circles denoting the resolved portion, x's showing the sub-grid portion, and the solid line marking the total amount ('o' + 'x'). These results
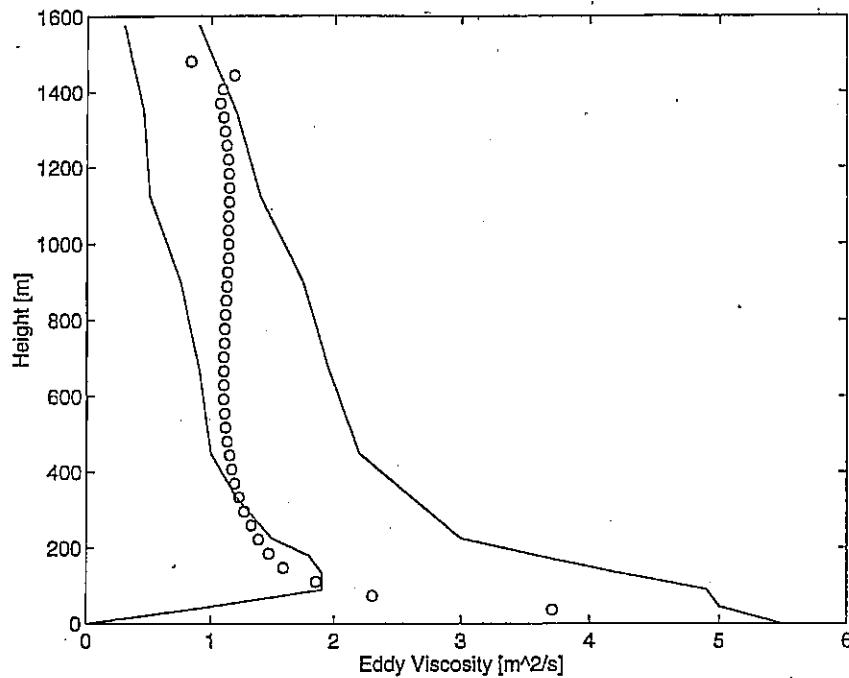
Figure 3.6: Vertical profile of eddy viscosity 'o', scaled with u_*z_i to put in dimensional form to compare with the range of results from Andren et al. (1994), which fall between the solid lines.

are nearly an exact match to those in A94. Consequently, the A94 results have been omitted from the figure for clarity. The constant mean streamwise pressure gradient at each height should theoretically result in a constant divergence of the stress at each height, from the maximum near the wall to a vanishingly small value at the stress-free lid – which is just what the simulation is showing.

The velocity power spectra should approach a power law scaling of $k^{-5/3}$ for wavenumbers much smaller than the production scales, in keeping with Kolmogorov's (1941) inertial subrange theories. It is common for LES codes to have extreme difficulty achieving this spectral behavior, such as the k^{-3} scaling found
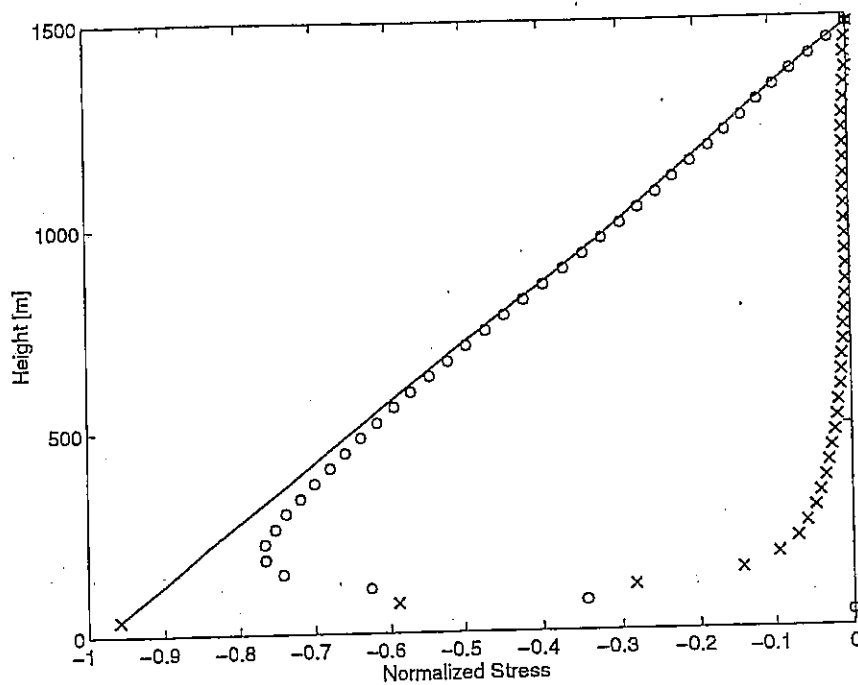
Figure 3.7: Profile of vertical turbulent flux of x-momentum (i.e stress) in dimensionless form. The resolved flux ($\overline{uw}$) is marked by 'o', the sub-grid flux is marked by 'x', and the sum of these two components is the solid line.

by Avissar and Liu (1996), while yet others have achieved this scaling with even low resolution LES, as in the 64^3 node simulation of homogeneous turbulence by Briscolini and Santangelo (1994). However, spectral scaling arguments have also been made for the low wavenumber, or production, range of scales. Tchen (1953) proposed that wall-bounded shear flows should possess a universal production spectrum which scales as k^{-1}, based on order of magnitude analysis of the Navier-Stokes equations. Perry and Abell (1975) found this scaling to exist in their pipe flow experiments and, later, Perry and Chong (1982) tied this scaling to the attached

eddy hypothesis of Townsend (1961, 1976). Extensive observations of the k^{-1} spectrum in the ABL were made by Katul et al. (1995); see this last paper for a review of the literature with respect to these scaling arguments. For the low resolution simulation of this chapter, with the partial dealiasing, the highest wavenumbers retained represent eddies still large enough to be strained by the presence of the wall. This local anisotropy would preclude the presence of an inertial subrange for all but perhaps the highest wavenumbers, and the bulk of the spectrum would be in the so-called production range. The one-dimensional power spectrum of the longitudinal velocity fluctuations is shown in Figure 3.8.
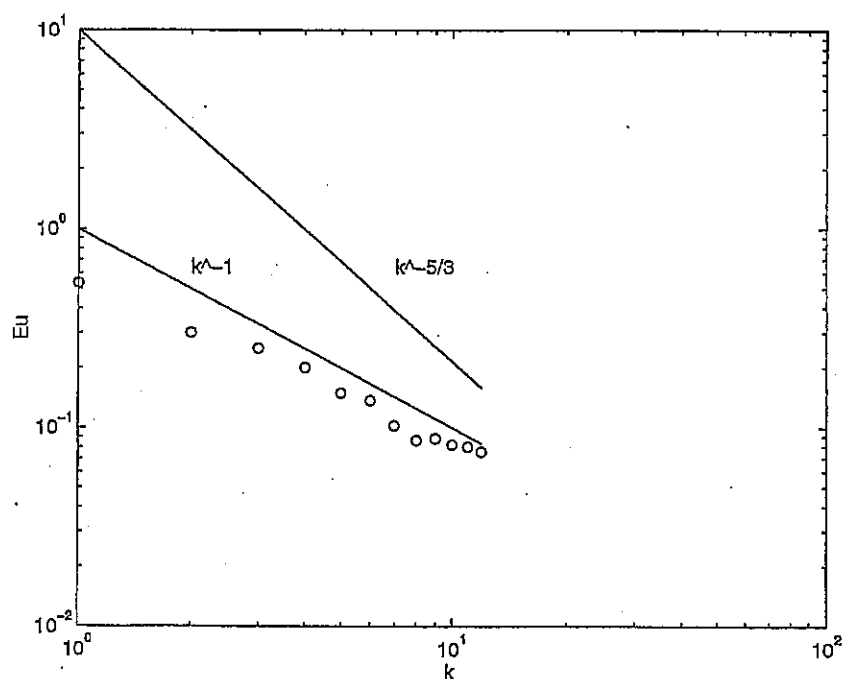
Figure 3.8: One-dimensional power spectrum of $\overline{u}_1$. The Kolmogorov inertial subrange scaling of $k^{-5/3}$ and the production range scaling of k^{-1} are shown for comparison.

This spectrum represents the $\overline{u}_1$ field at a single time and is averaged over all y and a range of z between 200 and 400 m. Note that the spectrum scales in accordance with the predicted k^{-1} scaling for the production range of a wall-bounded shear flow.

3.5   Conclusions

From this comparison study we have demonstrated that the present LES code, even with extremely coarse resolution, is capable of simulating velocity fields with means, variances, and stress distributions that compare reasonably well with published simulation results. Moreover, we have shown that for the most immediate purpose of studying the structure of the downward turbulent momentum flux in the ABL, this code performs extremely well. On the other hand, it was established that additional work is required to optimize the sub-grid model with respect to the Smagorinsky constant and perhaps the sub-grid length scale. It was suggested that this optimization may serve to reduce the magnitude of resolved velocity fluctuations in the outer region in order to better match the published results.

The power spectrum of the simulated velocity field was shown to match the scaling found from physical measurements at equivalent scales of motion in the ABL (Katul et al., 1995).

Now we proceed in Chapter 4 to increase the resolution and study ABL flow over a patchy land surface toward the stated objectives of this work.

CHAPTER 4

The Effect of Surface Patch Scale on Areal Averaged Surface Stress

4.1 Introduction

Whether modeling surface hydrologic processes or atmospheric processes the degree of success will depend largely on the ability to account for exchange across the land-atmosphere interface. A major concern for both the atmospheric and surface hydrologic models is how to account for the effect of the spatial variability of surface conditions on scales smaller than the model grid cell. The actual total grid cell exchange is an integration of small scale exchange processes over the area of the cell, where the integration is provided by the turbulent mixing in the ABL. There is at present no consensus on what measures of sub-grid cell surface properties are needed to represent the total exchange.

To begin to develop a general answer to these questions demands a vast amount of data covering (i) surface conditions over a range of scales of variability, (ii) surface fluxes distributed in space and time over the study area, and (iii) the dynamics of interaction between the surface and the atmospheric motions. Here we achieve this through the application of our new three-dimensional numerical simulation code. With analysis of the distributed (in space and time) simulation results we explore the interdependence of adjacent surface patches and the behavior of the actual aggregation up through the boundary layer over a range of spatial scales. The LES provides the ability to modify certain important characteristics

(e.g. length scale of surface patches) such that we can quantify their effects on the ABL structure and areally averaged exchange rates. This is a significant departure from the conceptual modeling approaches (e.g. Famiglietti and Wood, 1995) in that the simulation code represents the turbulent flux and transport through an implementation of the Navier-Stokes equations on a three dimensional grid over the study site. Therefore, the surface exchange and the turbulent mixing processes that combine to form the physical aggregation are represented by the basic equations, rather than through conceptual models.

Here we simulate momentum exchange across a patchy surface with LES, study how the flow couples the flux processes of the adjacent patches, and discuss implications for areally averaged exchange rates.

4.1.1 Surface Properties in Simulations of Hydrology and Meteorology In simulating hydrologic and atmospheric processes we need some measure of surface properties in order to estimate the total exchange across the land-atmosphere interface over the surface area of each grid cell. However, the open question is what measures are most important for an accurate and parsimonious representation of the averaged exchange processes.

Scales of Interest Studies of sub-grid heterogeneity in the context of general circulation models (GCM) have focused on patches at the mesoscale, with length scales of say 10 to 50 km. However, for physical hydrologic modeling of large catchments or regional climate analysis we are concerned with the effect of spatial variability

on length scales below say 2 km, as the grid cells may be of order 10^2 m to 10^4 m on a side. There is a natural gap in scale between these mesoscale patches and the local patches (scale < 2 km), for while the ABL adjusts fully to each of the mesoscale patches (e.g. Raupach, 1991), the flux from the local patches is integrated or mixed through the ABL with coupling between patches limited to the surface layer. The ABL thus represents the composite effect of the local patches, including the nonlinear interaction between the patches. The surface layer flow over the patches serves to couple the flux processes over one patch to those over the adjacent patch. Therefore, in keeping with the motivation of regional scale hydrology, the scope of this project is limited to scales of surface heterogeneity below 2 km and to the effect of these patches on the areal averaged exchange across the land-atmosphere interface.

Prevailing Methods   At present most numerical models of surface hydrologic processes and atmospheric processes typically account for the land-atmosphere exchange through the use of simple statistics of the surface properties. A first, and rather rough, approach to this problem has been to apply a simple linear aggregation (averaging) of the surface properties for use in estimating average grid cell exchange. These average properties are then used to estimate the average flux – an approach which ignores, by necessity, all nonlinearity and spatial coupling of the processes. A second approach, motivated by recognition of the nonlinear nature of the exchange processes, has been to compile a distribution function of each surface property within each grid cell and map these through surface exchange functions

in order to compute an estimate of the total grid cell exchange (e.g. Avissar, 1991, 1992). However, this approach assumes that the individual surface properties (e.g. roughness, temperature, and soil moisture) are uncorrelated as well as assuming that the surface patches are independent of each other. There is a bounty of experimental evidence to the contrary (e.g. Brutsaert and Stricker, 1979; Parlange and Katul, 1992), for it is known that local advection provides a strong coupling between adjacent patches on the land surface.

Frustrating efforts so far is the lack of a general understanding of the physics of land-atmosphere interaction over heterogeneous surfaces. Rather than a statistical approach, attention needs to be paid to the physics and how they scale. Here we address these questions through simulations with LES and systematic analysis of the physical processes that are interacting and combining to form the aggregate exchange.

In summary, the problem with the present approaches is that they ignore potential effect of scale on exchange, and dependence between adjacent patches. For example, the two cases in Figure 4.1 may at once have the same probability density function (pdf) of surface properties and yet have different total surface flux over the domain because of coupling between the patches and effects of length scale of the patches on the aggregate flux.

Coupled processes and the effects of scale   We know something about how the portion of the atmosphere closest to the surface reacts to a step change in surface properties, as encountered between landscape patches such as in the central val-
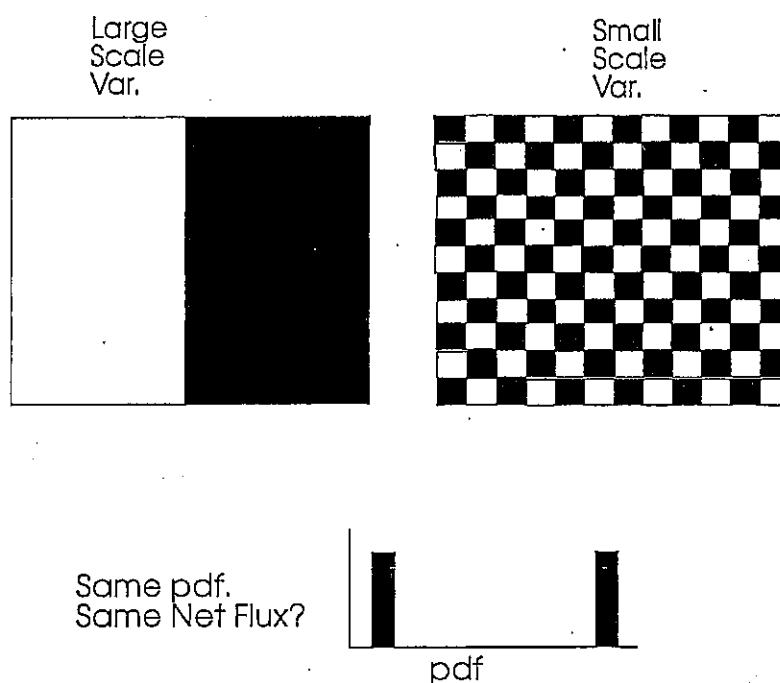
Figure 4.1: Two hypothetical surfaces with identical pdf's of surface properties, but different patch length scales.

ley of California. An internal boundary layer (IBL) forms just above the surface downwind of the interface. For a general review of the structure of the IBL see Garratt (1990). In order to develop modeled solutions for how the air mass responds to the step change in surface roughness, it has been necessary to introduce simplifying assumptions of questionable validity – such as the use of a predefined wind profile in the Kármán-Pohlhausen solution (see Elliot, 1958). For example, Townsend (1965a,b; 1966) assumed self preservation of both the wind profile and the shear stress. These solutions all employ closure of the Reynolds averaged equations. Brutsaert (1982, p. 164) points out that the solutions employing closure at level N typically disprove the assumptions used in solutions employing closure at

level N-1, thus casting doubt on the validity and generality of the solutions.

In a seminal field experiment, Bradley (1968) used artificial roughness elements and measured mean shear stress versus distance from a step-change in roughness with drag plates. He found the stress to equilibrate by about 2 m following the smooth-to-rough transition and 4 m following the rough-to-smooth transition. He compared the results to the theory of Panofsky and Townsend (1964) and found good comparison for the rough-to-smooth case. It is important to note that Panofsky and Townsend (1964) work in a dimensionless fetch of X/z_o, so we should scale the 2 m result by z_o before comparing to other cases. Bradley's (1968) experiment had estimated momentum roughness lengths of 0.00002 m over the smooth surface and 0.0025 m over the rough. The 2 m response over the rough surface corresponds to a dimensionless fetch X/z_o of $O(10^3)$. The Panofsky and Townsend (1964) theory was developed with consideration of the rough-to-smooth transition, but they remarked that "all theories can also be applied to the reverse situation by making the corresponding changes." Bradley noted that the rough-to-smooth equilibrated faster than the reversed case, but did not address possible reasons. This asymmetric response is central to our problem.

Antonia and Luxton (1971) used wind tunnel data to study the structure of the IBL after a step change in surface roughness from smooth-to-rough. They found that this boundary layer reached a "second self-preserving state on the rough wall well downstream of the roughness step." The IBL was found to grow at a rate similar to the zero pressure gradient boundary layer, with the growth rate

controlled by the diffusion of TKE from the high production region near the surface.
They studied the change in surface stress with distance from the edge using profile
drag measurements from pressure taps on the roughness elements, and found that
a new equilibrium surface stress was reached at a distance well downstream of
the transition. In a subsequent study of the transition downstream of a rough-
to-smooth transition Antonia and Luxton (1972) found strikingly different results.
Over the smooth surface the transition to a new equilibrium took much longer, with
the rate of growth of the IBL being markedly less than downstream of the smooth-
to-rough transition. They note that this agrees generally with Bradley's (1968)
observations. The slow growth of the IBL over the smooth surface is attributed
to influences from both the inner and outer layers. In contrast to the smooth-to-
rough case, where the upward diffusion of TKE (in the internal region) controls the
growth rate, the IBL growth rate following a rough-to-smooth transition is damped
by the outer region's action to compensate for reduced production of TKE over
the smooth wall. Hence the response for rough-to-smooth may be due to both the
internal and outer regions, while the response in the reverse case may be due to
solely the internal region processes.

Rao et al. (1974a) studied the growth of the IBL in a neutral boundary layer
after a step change in roughness with a numerical model of the Reynolds averaged
equations and a full turbulence closure scheme. Their results generally match
the experimental results of Bradley (1968) for the same small roughness lengths.
In an application of an extended version of their model, where water vapor and

temperature are modeled as well, Rao et al. (1974b) found the Bowen ratio (latent heat flux : sensible heat flux) to respond to a step change in surface wetness at a similar rate as the surface stress responds to a step change in roughness.

Weisman (1974) continued the work of Weisman and Brutsaert (1973) to study the IBL forming over an evaporating lake with equivalent surface roughness to the surrounding land. The distance from the shore was non-dimensionalized by z_o, in recognition of the effect of surface roughness on the rate of response to the step change in surface conditions. Weisman's (1974) model predictions show noticeable surface flux variation through a distance from the leading edge of at least $10^3 z_o$ to $10^4 z_o$. McNaughton's (1976) theoretical development also recognized the dependence of surface flux response on the roughness length and his results show effects on surface fluxes of water vapor over reaches at least as far as Weisman's.

Several other recent studies have employed Reynolds averaged models of the surface layer, with various closure models for the full turbulent field, to address the issue of how patches on the surface interact to produce the aggregate large scale surface fluxes (e.g. Claussen, 1991; Klassen, 1992; and Kroon and deBruin, 1993; and Baldocchi and Rao, 1995). These authors have noted the edge effects due to the presence of the upwind field and postulated how these effects will influence the aggregate exchange over a larger area. However, with these Reynolds averaged approaches all of the variability in surface exchange is brought about by variations in the mean longitudinal velocity caused by the transitions in surface properties. Here we simulate the three dimensional turbulent motion and transport with vari-

ation in time and space, such that the surface stress develops a time and space distribution as a consequence of both the mean field and the turbulent field.

<u>4.1.2 Rationale and Objectives</u> For the range of scales of present interest it would seem that there are three separate regimes for consideration in aggregation: the largest patches, which are mostly in equilibrium with the flow and may be treated independently of each other; a mid-range of scales which have a significant portion of their area in the transition region affected by the adjacent patch and must be considered as coupled patches; and, the small patches, which can not significantly affect the flow properties over an individual patch and may be treated statistically.

<u>Scientific Rationale</u> The rationale for the present approach is that the LES provides physically realistic three dimensional images of the ABL structure over patchy land surfaces to reveal both spatial and temporal details of the atmospheric response to surface features. This work is motivated by the need for better parameterizations of river basin scale surface fluxes. Moreover, the physical simulation and analysis of how surface patches interact with each other through the surface layer coupling holds promise for providing a physical basis for limiting the scales of surface heterogeneity which must be treated explicitly for predicting basin-scale land-atmosphere interaction.

<u>Objectives</u> The specific objectives of this study are to:

1. Identify spatial coupling between surface patches.

2. Identify the effect of patch scale on spatially averaged exchange rates.

3. Explore possible implications from the momentum case for scalar exchange.

4.2 A Suite of Simulations

4.2.1 Approach In support of the objectives listed above a suite of three ABL simulations was performed over patchy surfaces of varying patch length. The LES code simulates the turbulent eddies and their transport effects that serve to couple the patches. By varying the length scale of the patches we are able to investigate how the scale of the surface heterogeneity affects the structure of the flow and what ramifications it has for the total domain aggregated surface exchange of momentum.

4.2.2 General Flow Description While the patch scale varies between the three simulations, all other gross flow characteristics remain unchanged. The depth of the simulation domain is 700 m. The scaling height was chosen as $z_s = 500$ m, such that the horizontal dimensions of the domain are 3140 m (i.e. $2\pi z_s$) in each the x and y directions. The mesh is staggered as described in Chapter 2. The domain is spanned by 64 nodes in the x-direction, 32 nodes in the y-direction, and 100 nodes in the z-direction, such that the nominal dimensional mesh spacing is 50 m in the x-direction, 100 m in the y-direction, and 7 m in the z-direction. Note that because of the staggered mesh the first plane of nodes above the wall for u and v is at $\Delta z/2 (= 3.5 \ m)$.

The initial conditions are prescribed similarly to those in Chapter 3, save the

changes in the vertical length scales. For completeness the explanation is repeated here in summarized form. The initial conditions are a modified logarithmic velocity profile with a prescribed TKE profile superimposed on the mean profile. The mean profile is logarithmic in the surface layer, but is forced to reach a zero vertical gradient at z_s and remain at a constant velocity above this height. This was achieved through integration of

$$\partial_3 < \overline{u}_1 >= \frac{1}{kz} - \alpha z; \quad z \leq 1 \ (= z_s/z_s) \tag{4.1}$$
$$\partial_3 < \overline{u}_1 >= 0; \quad z > 1$$

with α selected to force the gradient to vanish at z_s. This yields a mean velocity profile of

$$< \overline{u}_1 >= \frac{1}{k}\ln(z/z_o) - \frac{\alpha}{2}z^2; \quad z \leq 1 \tag{4.2}$$
$$< \overline{u}_1 >= \frac{1}{k}\ln(1/z_o) - \frac{\alpha}{2}[1]^2; \quad z > 1$$

where $z_o \ (= 0.1m/z_s)$ was selected to correspond roughly to an effective roughness (Claussen, 1991) representative of the overall effect of the patchy surface, which is described below. The initial transverse and vertical velocities have zero mean values at all heights. The initial vertical profile of resolved TKE is again taken from Andren et al. (1994, Table A.1). The instantaneous velocities $\overline{u}_i(x, y, z)$ are obtained by distributing the TKE randomly between the components and randomly in space onto the mean profiles.

A dimensionless time step of 0.0005 was used, which corresponds to a dimensional time step of roughly 1/2 second. The spinup period was chosen to be 10,000

time steps for each simulation, corresponding to 5 dimensionless time units or a physical period of roughly 1.4 hrs. The statistics for the comparison below were computed over a simulation period of 3000 time steps (e.g. 1/2 hour of physical turbulence), immediately following the spinup period. For each of the three simulations the spinup was satisfactorily long to yield stationary statistics through the 3000 step analysis period. We observed these simulations to reach a statistically stationary state significantly sooner than that of Chapter 3.

4.2.3 Varying Surface Properties The simulations are of turbulent ABL flow over surfaces of patchy roughness. In all cases the patches alternate between smooth and rough, starting with a smooth patch at x=0. The roughness fields are homogeneous in the y direction (i.e. lateral stripes of constant roughness). The dimensional momentum roughness length is 0.025 m for all of the smooth patches and 0.25 m for all of the rough patches; the transitions between the patches is perfectly abrupt. Boundary conditions are as described in Chapter 2.

4.2.4 Case Comparison The sole difference between the three simulations studied is that: Case I has two surface patches (i.e. 1 smooth and 1 rough), Case II has four patches, and Case III has eight patches. The length scales of the individual patches are 1570 m for Case I, 785 m for Case II, and 390 m for Case III. In the following section we will first explore some basic results from the simulations and then examine the effects of the patchy surface roughness on the structure of the flow and on the areally averaged exchange rates. Where appropriate, ties will be drawn to the literature reviewed above.

4.3 Results and Discussion

This section will begin with a look at the general behavior of the simulated boundary layer turbulence and will then move to an examination of the response of the turbulent flow to spatial variations in surface roughness, including a detailed comparison of the three simulation cases.

In this chapter we are concerned with the surface stress due to the downward flux of momentum to the land surface from the ABL flow. In the boundary layer this downward flux manifests itself in a negative correlation between the longitudinal and vertical velocity fields. We see this relationship in Figure 4.2 by examining a time series of the U/u_* $(=\overline{u}_1)$ and W/u_* $(=\overline{u}_3)$ velocity components at a single node in the flow. This figure is also instructive in that it depicts the large scale nature of the resolved velocity, as established in Chapter 2 with the filtering. Note that the smallest time scales of the motion appear to be several tens of seconds. The negative correlation between these two time series is evidence of the downward flux of momentum through this point. For example, the first 100 seconds of the series shows a higher than average longitudinal velocity as the fluid is generally moving downward $(U' > 0, W < 0$; i.e. a "sweep"), and the second 100 seconds shows a lower than average U as the fluid moves upward $(U' < 0, W > 0$; i.e. an "ejection"). See Raupach et al. (1991) for a clear and thorough discussion of momentum flux in rough wall boundary layers.

Figure 4.3 depicts how the resolved longitudinal velocity fluctuations scale with respect to eddy size, that is, in the wave domain. The spectrum is computed from
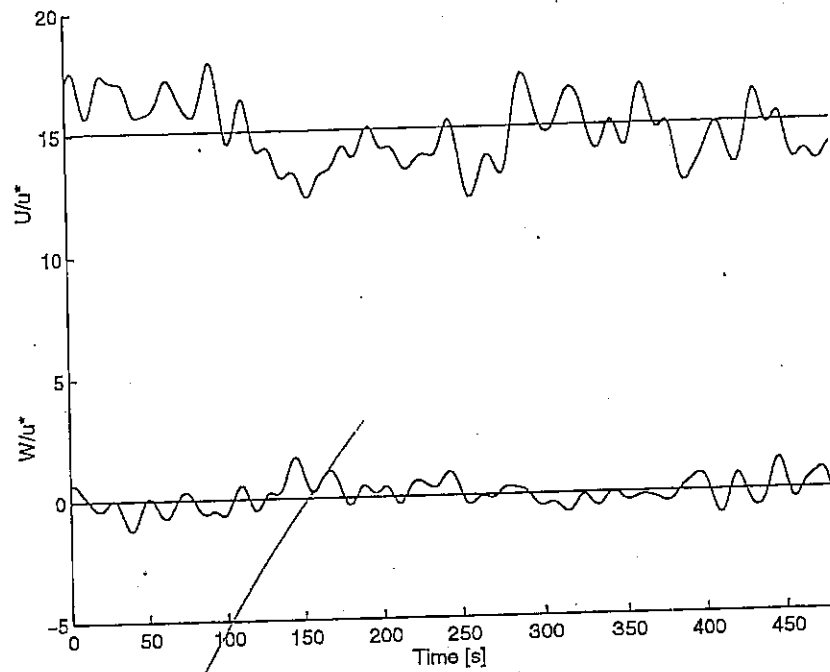
Figure 4.2: Time series of U/u_* and W/u_* at a single node located 4.5 Δz above the wal for U and $4\Delta z$ for W. Horizontal lines mark the time averaged values of the two velocity components.

one-dimensional Fourier transforms in the x-direction, which are averaged over all y positions and three levels of nodes in z located near the top of the surface layer. The numerical values on the k axis represent the number of full waves of size k that would fit inside the x-direction extent of the domain. The majority of the velocity variance is in fact held by the large scale motion (low wavenumbers) which is scaling with the k^{-1} slope as described in Chapter 3 and the smaller resolved scales ($k > 10$) do appear to be approaching the power law scaling $k^{-5/3}$ representative of Kolmogorov's (1941) inertial subrange. Thus the simulated turbulence meets two important, necessary, but not sufficient, conditions for a fully developed turbulent

flow (see Tennekes and Lumley, 1972).
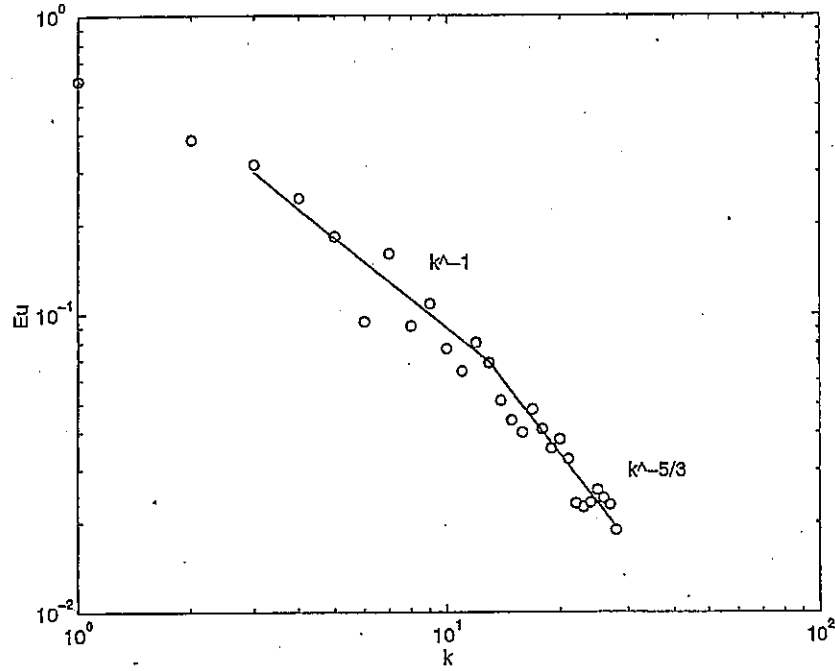
Figure 4.3: One-dimensional power spectrum ('o') of the longitudinal velocity fluctuations at a single point in time averaged over all y and a range of three levels of z in the surface layer. The k^{-1} production range scaling and the Kolmogorov (1941) $k^{-5/3}$ scaling for the inertial subrange are marked with solid lines.

The correlation between the $\overline{u}_1$ and $\overline{u}_3$ fields, as manifested in Figure 4.2, is shown clearly in the joint pdf of these two variables in Figure 4.4, based on observations of $\overline{u}_1$ and $\overline{u}_3$ through the full simulation time and the full horizontal extent at $z = 5\Delta z$. Note that for the pdf's we use U'/u_* and W'/u_* to represent fluctuations of the dimensionless resolved scale velocity from the local time averages of $\overline{u}_1$ and $\overline{u}_3$. The correlation between these two fields is marked by the elliptical

nature of the pdf and the downward direction of the momentum flux is marked by the negative slope of the major axis of the ellipse. The events captured in the upper left quadrant of the plot represent the "ejection" of low momentum fluid upward, and the events in the lower right quadrant are from the "sweep" of high momentum fluid downward.
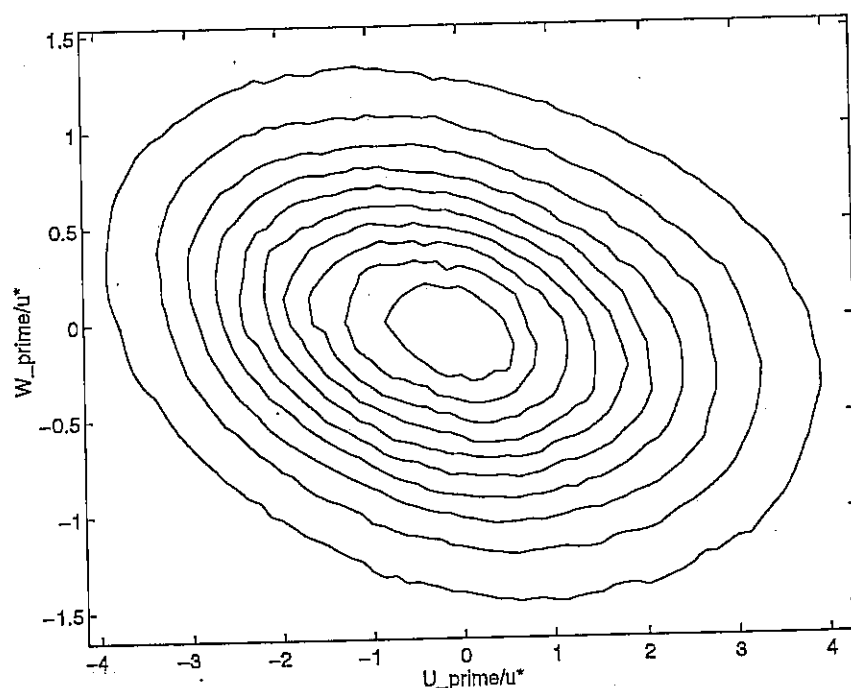

Figure 4.4: Joint probability distribution of U'/u_* and W'/u_*. The lines denote equal probability and are separated by a constant increment.

The single variable pdf's of U'/u_* and W'/u_* are shown in Figures 4.5 and 4.6. For comparison a Gaussian is drawn in each of these two figures with a solid line. Note that as expected for a neutrally stratified shear flow the resolved velocity fluctuations are close to Gaussian. The slight departure from Gaussianity that is present can be described as a minor positive skewness in the U' statistics and

the appearance of a minor deviation in flatness factor from the Gaussian value of 3 in the W' statistics. These statistics are taken over the same physical region as those in Figure 4.4. See Nakagawa and Nezu (1977) and Katul et al. (1996) for a discussion of the statistical structure of the Reynolds stress and arguments explaining departures from Gaussianity.
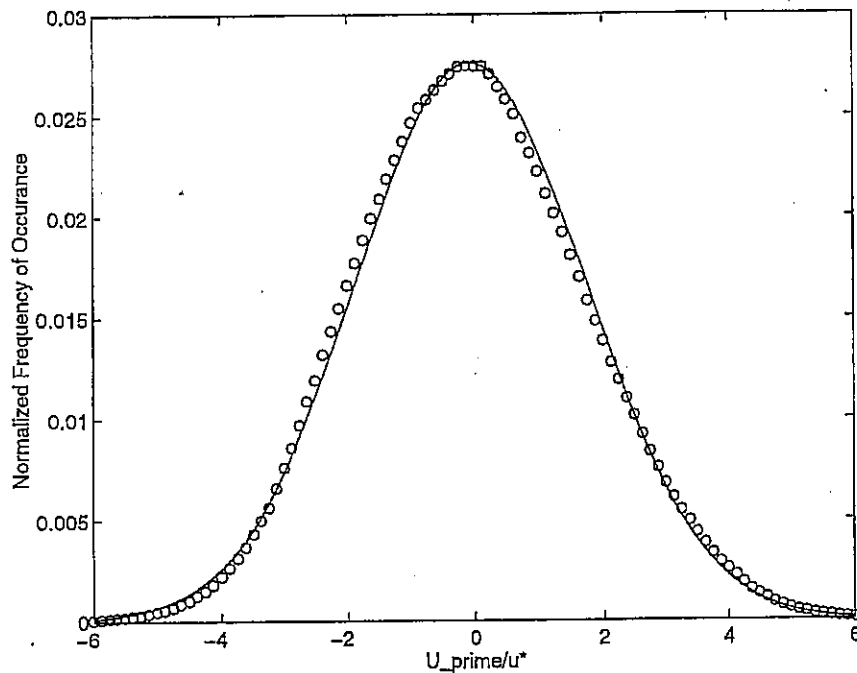

Figure 4.5: Probability density of U'/u_* ('o'), with a normal distribution drawn with a solid line.

An instantaneous vertical cross section of the $\overline{u}_1$ field is shown in Figure 4.7 to provide a spatial image of the sweep and ejection process, whereby momentum is transported (in a net sense) toward the land surface. Note the excursions of low momentum fluid (dark) into the outer regions and the sweeps of higher momentum
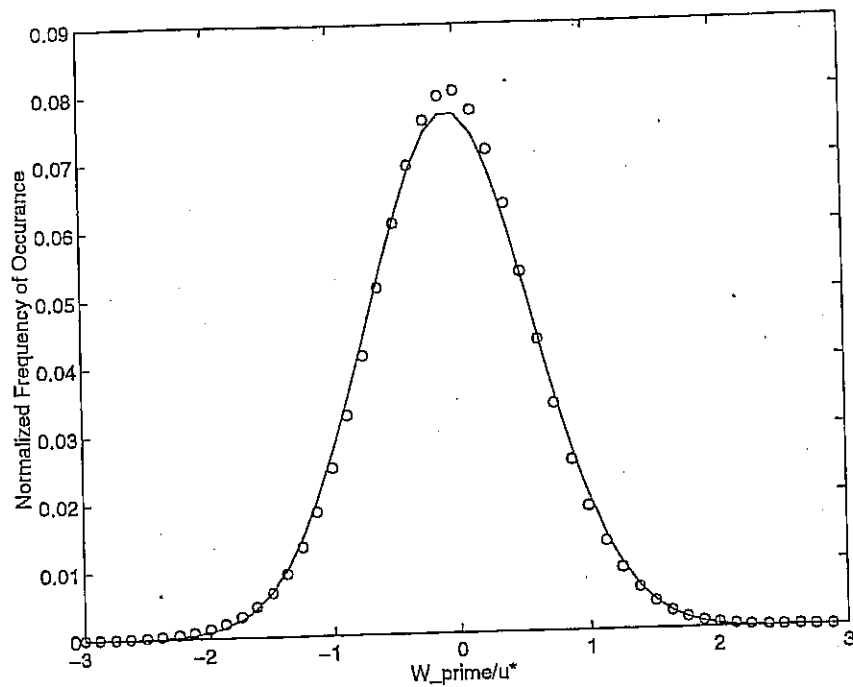
Figure 4.6: Probability density of W'/u$_*$ ('o'), with a normal distribution drawn with a solid line.

fluid (light) into the near wall region. The surface stress, which is our focus in this chapter, is the ultimate representation of this momentum flux across the surface interface.

The instantaneous resolved stress (or momentum flux) and the instantaneous sub-grid stress are combined and averaged in time and over the y-direction to provide a time averaged picture of how the total downward momentum flux is affected by the presence of the patchy surface roughness. Figure 4.8 shows the structure of the normalized stress (or downward momentum flux divided by squared friction velocity) over the x and z directions for the four surface patches of Case II. The first and third patches from the left edge of the figure are smooth and
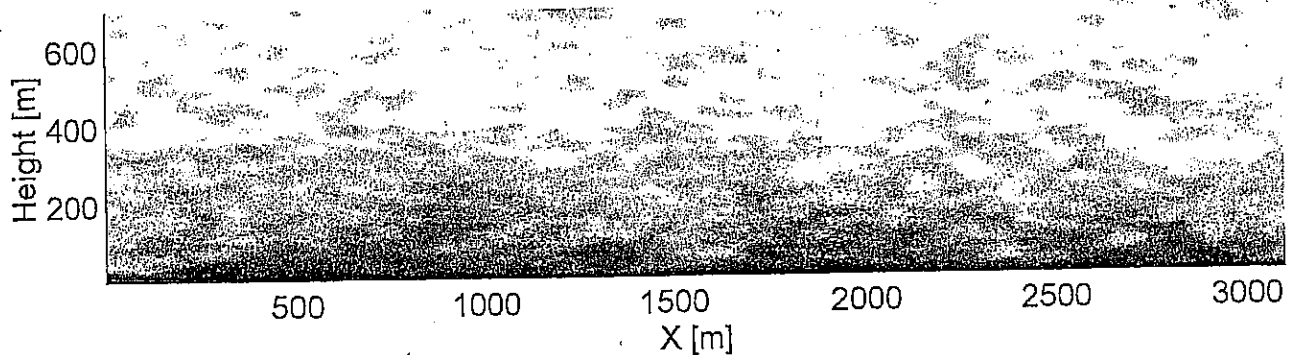
Figure 4.7: Instantaneous vertical cross section through the U field. Dark colors are low velocity and light colors (to white) are high velocity fluid.

the second and fourth are rough. The flux over the leading edge of each patch is affected through the dynamics of the flow by the presence of the upwind patch. The near surface fluid is moving faster on average over the smooth patches than over the rough patches, so as it moves from smooth to rough there is an increased stress over the leading edge, which is steadily diminished as the fluid slows to the rough patch equilibrium. Over the leading edge of the smooth patch the fluid is moving slow from the effect of the upwind rough surface, causing the reduced stress which is steadily increased as its smooth surface equilibrium value is approached.

Having established the general behavior of the simulated flow we proceed to examine and compare the three cases in the context of the stated objectives.
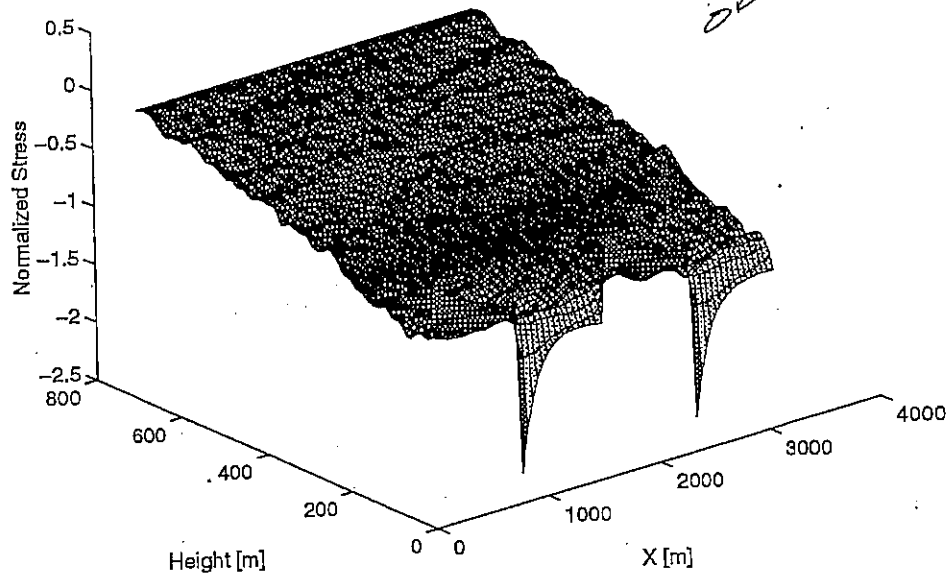
Figure 4.8: Total vertical turbulent flux of x-component momentum (sub-grid plus resolved) for Case II.

The streamwise structure of the longitudinal velocity ($\overline{u}_1$) averaged over y and t at the first node level above the wall ($z=\Delta z/2$) is shown for the three cases in Figure 4.9. There are two important features to note from this figure: (i) how the transition region, in which the velocity is significantly different from its equilibrium patch value, represents a relatively larger portion of the total patch size for the small patches; and, (ii) how the rough patch equilibrates faster than the smooth patch.

We study this second point in more detail with Figure 4.10, where from the Case I results we plot the difference between the time averaged streamwise velocity and its equilibrium value for each the smooth and rough patches versus distance
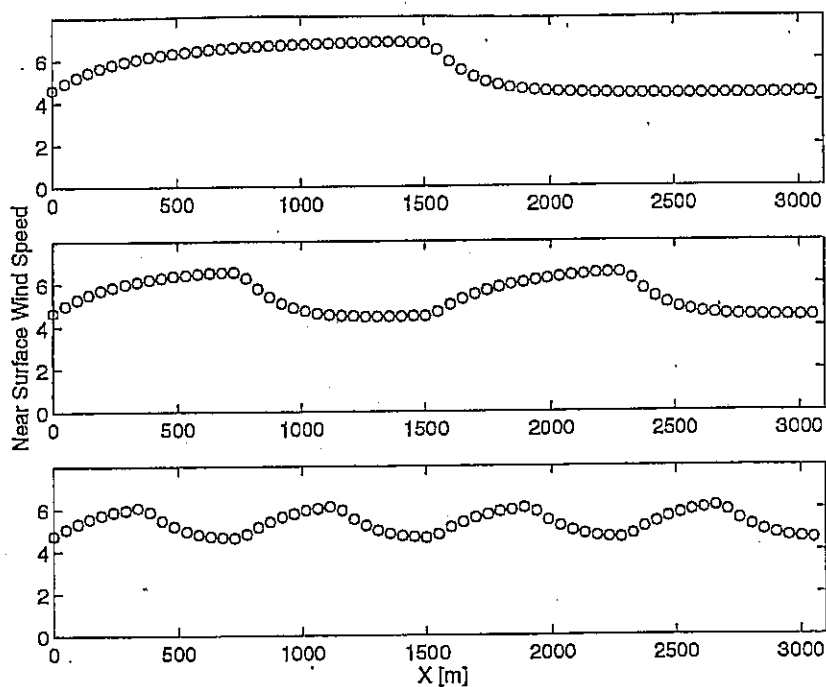
Figure 4.9: Mean longitudinal velocity at $z=\Delta z/2$. Case I is on the top panel, Case II on the middle panel, and Case III is on the lower panel.

from the leading edge of the patch. The circles were obtained by subtracting from the rough patch series of Figure 4.9 the value that the streamwise velocity asymptotes to over the rough patch, hence in this form it asymptotes to zero; the x's were obtained similarly, but for the smooth patch; and the solid line is the difference between the two derived series. Case I is used here to show the structure of these series over extended fetch from the transition. Note from comparing the cases in Figure 4.9 that Cases II and III are well represented by the left side of Figure 4.10, since (with respect to near surface averaged wind velocity) these two cases are mainly foreshortened versions of the longer case. This asymmetric trend toward equilibrium was noted in the wind tunnel experiments of Antonia and

Luxton (1971, 1972). One important qualification needs to be made here: Antonia and Luxton's smooth wall is truly "smooth" in the fluid mechanics sense of the term, whereas we are studying what is technically a rough-to-rough transition where the magnitude of the roughness changes at the interface. Nonetheless, their observations are qualitatively similar to the present ones derived from LES and their explanations for the asymmetry of response seems equally relevant to the present case. It is encouraging to note that the LES, through simulating the interaction of the turbulent boundary layer and the wall, is capable of capturing this effect. Note from the solid line that the departure from equilibrium is nearly everywhere greater over the smooth patch than over the rough patch. With the LES results it is possible to tie this result to the structure of the surface stress over the patches and to the relationship between the areally averaged surface stress and the length scale of the surface variability. We will discuss this below.

Figure 4.11 shows the corresponding longitudinal structure of the surface stress for Case II (averaged over y and t). Note that the positive non-equilibrium velocity increment (ΔU) over the leading edge of the rough patch translates into a much larger stress increment than does the slightly larger magnitude but opposite signed velocity increment over the smooth surface. This is due to the relationship between the squared near surface velocity and the surface stress. However, with LES we have the average surface stress arising from a time and space distribution of surface stress that is derived from the time and space distribution of the near surface velocity; that is, it is not a simple relationship between mean quantities as with
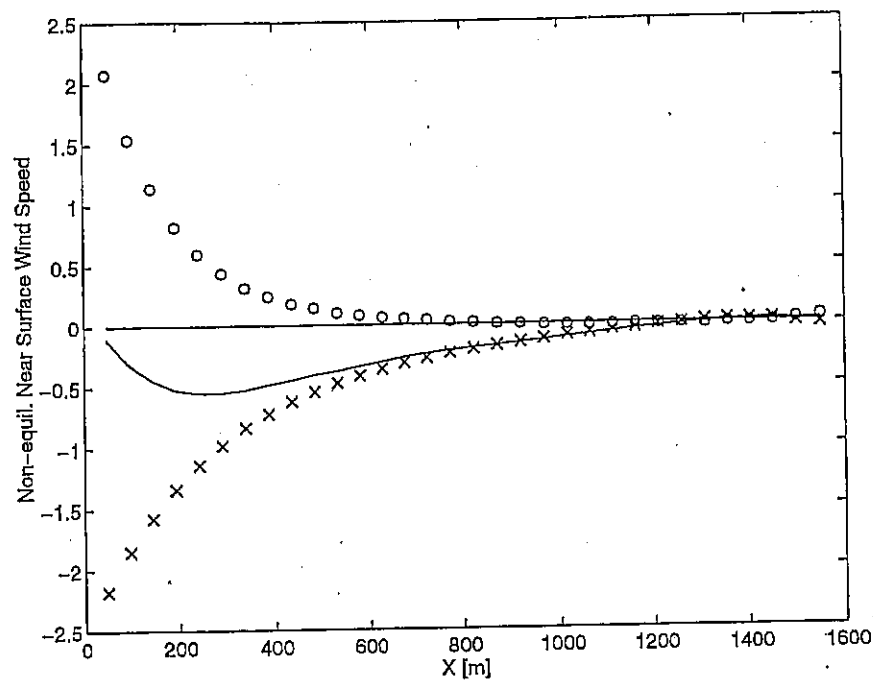
Figure 4.10: Difference between mean longitudinal velocity and equilibrium velocity over the rough patch ('x') and over the smooth patch ('o') versus distance from leading edge of the patch for Case 1. The difference between ('x') and ('o') is plotted with a solid line.

the Reynolds averaged models.

As a minor point, but encouraging with respect to the accuracy of the simulation, we observe that the slight decrease in stress just upstream of the smooth-to-rough transitions and the slight increase in stress just upstream of the rough-to-smooth transition is in qualitative agreement with the detailed analysis of the transition region performed with a stream-function vorticity model by Claussen (1987). On the smooth-to-rough transition this can be explained by the slower flow region over the rough surface acting as a barrier to the incoming flow. Just
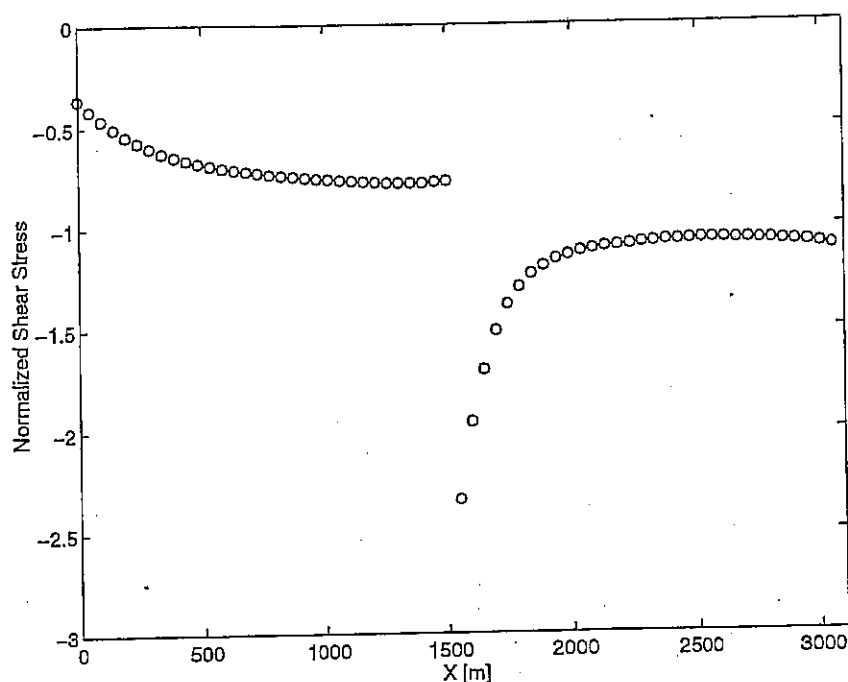
Figure 4.11: Variation in surface shear stress along the x-direction of the domain for Case I (averaged over y and t).

prior to the rough-to-smooth transition the fluid is beginning to speed up to maintain continuity with the faster flow over the smooth patch. Although Claussen's study focused on the region upstream of the step change, he did note that a new equilibrium stress was not yet reached by the end of his study region, a distance of $600z_o$ downstream from the transition (i.e. > 150 m over our rough surface).

In Figure 4.12 we compare the departures from patch equilibrium values for the stress over the rough and smooth patches in Case I (as with the velocities in Figure 4.10). Here we see a combination of effects: The slower trend toward equilibrium over the smooth patch is evident along with the accentuated effects on the stress at the leading edge from the positive velocity increments over the rough patch. This

gives rise to a difference between the non-equilibrium stress series (solid line) that
crosses the origin (unlike the velocity difference which was everywhere in favor of
the smooth patch). The leading edge has a larger non-equilibrium stress increment
over the rough patch, an equality is reached somewhat downstream of the leading
edge, and finally the amount over the smooth surface is greater over the interior
region of the patch. In effect, there is a partial canceling of effects when integrated
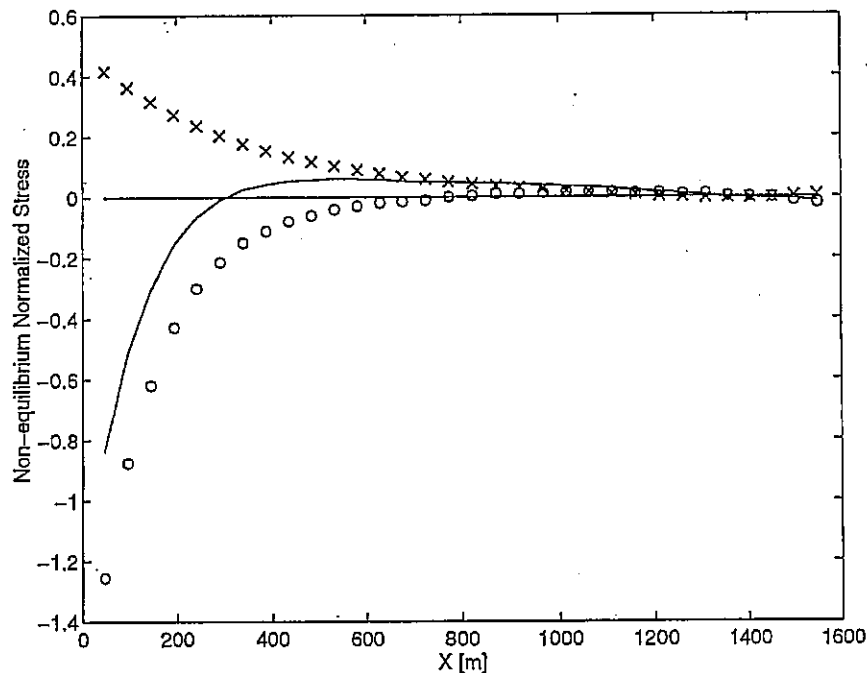over the full large patch.

Figure 4.12: Difference between mean surface shear stress and equilibrium
stress over the rough patch ('o') and over the smooth patch ('x') versus
distance from leading edge of the patch for Case I. Note that increasing
negative values imply higher stress. The difference between ('o') and
('x') is plotted with a solid line.

It is actually the sum of the two or the difference between the magnitude of(x) and the magnitude

This is explored with a running integration of the difference between the non-equilibrium stress with respect to x in Figure 4.13. For any value of x on this figure the ordinate marks the area under the solid line in Figure 4.12 to the left of x. Note that the maximum integrated non-equilibrium stress difference is found for a patch length of 200 to 300 m, and the total difference is realized by x ≈ 1000 m, such that the net stress difference from equilibrium does not increase for patch lengths greater than 1 km. It is should be restated that these results are intended to demonstrate the general effects of the patchy surface on the areal averaged exchange, but that quantitative interpretation of the fetch distances should be considered in terms of a distance variable normalized by z_o. For the present concern of shear stress, we note that Taylor's (1970) modeling results suggested a transition following a change in surface roughness extending several orders of magnitude greater than z_o — similar order of magnitude as seen here.

The response of the surface shear stress to the varying patch size of the three simulations is shown in Figure 4.14. As with the mean near surface velocity, the smaller patch cases appear as foreshortened versions of the long patch case. Therefore, the analysis in Figures 4.12 and 4.13 are general to all the cases, with appropriate truncation of the x axis. From Figure 4.14 it is apparent that the shorter patch cases have a larger fraction of their surface area in the transition region than the long patch case, which has an essentially constant stress over the majority of each patch.

Figure 4.15 shows the pdf of the surface stress as it varies over x,y, and t for
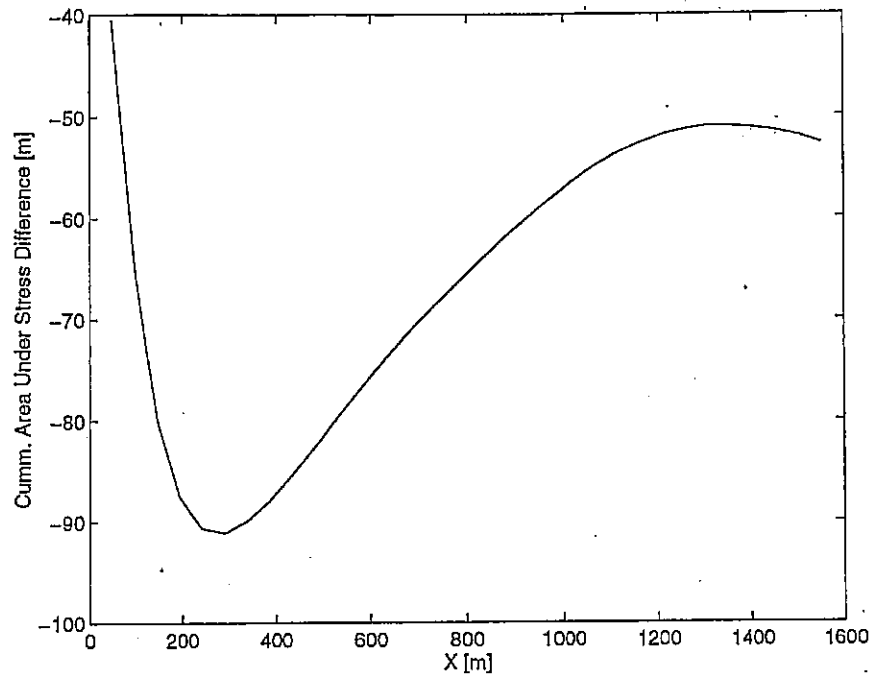
Figure 4.13: A running integration of the non-equilibrium stress difference between the rough and smooth patches versus the integration distance from the leading edge.

each of the three cases. The distributions widen as the patch size is decreased from Case I to Case III. This is explained by the increasing proportion of the domain affected by transition areas for the smaller patch sizes. Hence, there is a noticeable relationship between the length scale of surface roughness variability and the statistical structure of surface stress.

At its most simple form this relationship is marked by the dependence of the average surface stress on the length scale of the surface patch, as shown in Figure 4.16. The decrease in patch size is increasing the domain averaged surface stress, due to the interaction of adjacent patches through the coupling affected by the
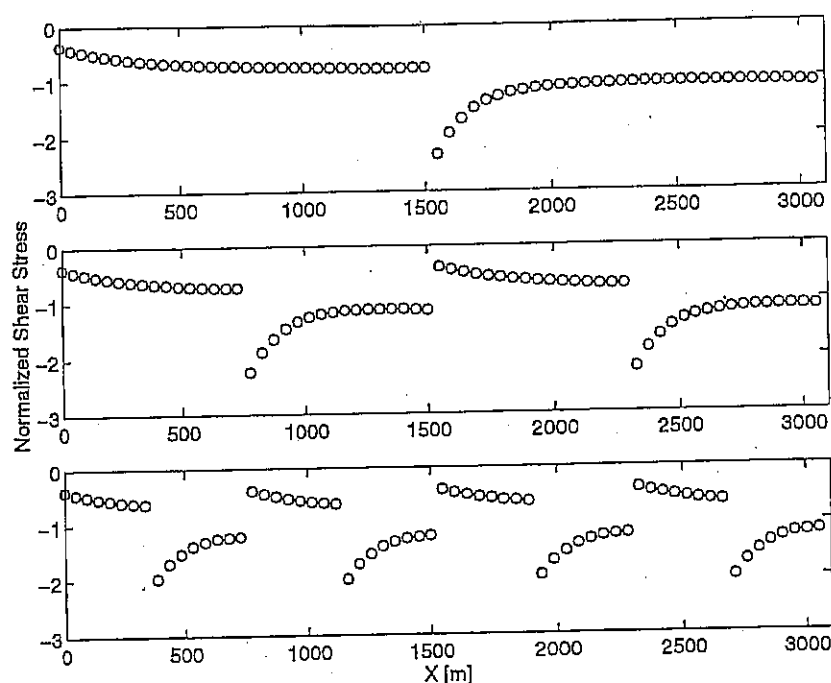
Figure 4.14: Mean surface stress versus x for each of the three cases.

surface layer turbulence and the asymmetric response noted above. Thus we see that, as hypothesized in the introduction to this chapter, surfaces with identical pdf's of surface properties are likely to have different areally averaged exchange rates.

The presence of patches of surface roughness is also noticed in the mean vertical component of the velocity. In Figure 4.17 the air is shown to be moving upward on average over the leading edge of a rough patch and to be moving downward on average over the leading edge of a smooth patch. This is due to the conservation of mass and the one-dimensional nature of the surface variability (i.e. homogeneous in y). The mean wind is slowing over the rough patch, i.e. $\partial_1 \overline{u} < 0$, which through the conservation of mass ($\partial_i \overline{u_i} = 0$) is creating an increase in the vertical wind
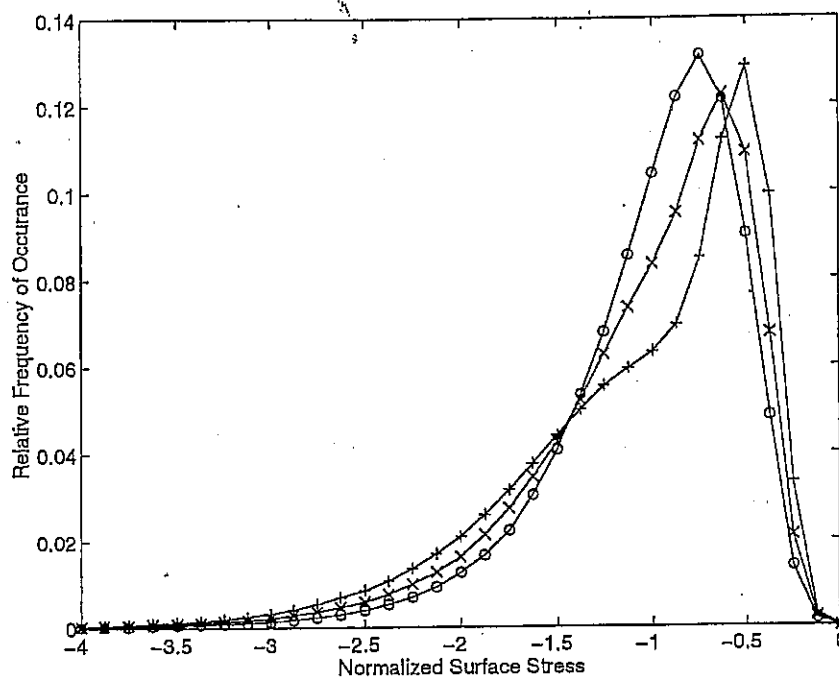
Figure 4.15: Probability density functions of the surface stress distribution (over x,y,t) for each of the three cases, with: 'o' for Case I, 'x' for Case II, and '+' for Case III.

velocity with height, $\partial_3 \overline{w} > 0$. The converse is occurring over the smooth patch.

The series of $z = \triangle z$ values from Figure 4.17 are shown in Figure 4.18 for closer examination of the near surface region.

These last two figures are included to highlight the implications for scalar flux near the leading edge of surface patches. Following the transition to a rough patch there may be enhanced upward scalar flux due to a combination of increased surface stress and the mean upward motion in this transition region. And, in the leading edge region of a smooth surface there is a reduced shear stress and a net downward motion serving to dampen the vertical turbulent flux.

Routine	Reads	Returns	Calls to
Fourn (Press)	In	Out	
Init_qprof		Q	
Init_rough		Zo	
Init_tprof		Theta	
I_point (func)	i,j,N_i	I_point	
Jointpdf	U,W	pdf,error	
Jointpdf_dz	U,W,	pdf	
Non_dim2d	A, Scale	A'	
Non_dim3d	A, Scale	A'	
Openfiles			
Pdftxz	txz	pdf_txz,error	
Press_stag	Rhs_x,Rhs_y,Rhs_z, Rhsx_f,Rhsy_f, Rhsz_f,u,w,w,divtz	P	slice1, fourn, Rpoint,Ipoint, Tridag, build1
Prof	A	Aprof	
Q_surf		Q_s2d	
Ran3 (Press)	idum	ran3	
Rem_ny	F	F	Slice1, Fourn, Rpoint,Ipoint, Build1
Replace	From	To	
Rms_div	du,dv,dw	rms	
Rough_patch		Zo	
R_point (func)	i, j, N_i	R_point	

Routine	Reads	Returns	Calls to
Scalar_rhs	s,u,v,w,Nu,txz,tyz, S_surf,z_os	Rhs, Sgs_vert	Ddx, Ddy, Ddz_uv, Ddz_w,
Scalar_rough	z_o	z_os	
Scalar_slice	w,t,q,sgs_t3,sgs_q3	at,aq,t2,q2,asgs_t3, asgs_q3,awt,awq	
Sgs_stag	dudx,dudy,dudz, dvdx,dvdy,dvdz, dwdx,dwdy,dwdz	Nu,Nu_bar	
Slice1	In, k	Out	
Stepbl_uv	ui,Rhsi,Rhsi_f,Force	ui	
Stepbl_w	ui,Rhsi,Rhsi_f,Force	ui	
Step_s	S,Rhs,Rhs_f,	S	
Stress_uvp	Nu,d1,d2	t	
Stress_w	Nu,d1,d2	t	
Tke	u,v,w	e	
Tridag (Press)	a,b,c,r,n	u	
T_surf		T_s	
Vel_ic		U,V,W	Ran3
Wallstress2	u,v,z_o	txz,tyz	
Zero1_pdf	pdf_txz,error	pdf_txz,error	
Zero2_pdf	pdf	pdf	
Zeroslices	au,av,aw,ap,u2,v2,w2 ,atxx,atxz,atyy,atyz, atzz,p2,auw,avw	au,av,aw,ap,u2,v2, w2,atxx,atxz,atyy,a tyz, atzz,p2,auw,avw	
Zero_pdf	pdf,error	pdf,error	
Z_sslices	at,aq,t2,q2,asgs_t3, asgs_q3,awt,awq	at,aq,t2,q2,asgs_t3, asgs_q3,awt,awq	